Description of the asymmetric to symmetric fission transition in the neutron-deficient thorium isotopes: Role of the tensor force

R. N. Bernard ⬤,[1,2,3,*] N. Pillet ⬤,[2,†] L. M. Robledo,[4] and M. Anguiano[5]

[1]*Department of Nuclear Physics, Research School of Physics and Engineering, Australian National University, Canberra, Australian Capital Territory 2601, Australia*
[2]*CEA, DAM, DIF, F-91297 Arpajon, France*
[3]*Ecole normale supérieure Paris-Saclay, 61 Avenue du Président Wilson, 94230 Cachan, France*
[4]*Departamento de Física Teorica, Universidad Autónoma de Madrid, E-28049 Madrid, Spain*
[5]*Departamento de Física Atómica, Molecular y Nuclear, Universidad de Granada, E-18071, Granada, Spain*

In the present study, we have investigated the impact of the tensor force on fission paths, in particular the symmetric and asymmetric barriers in ^{230}Th, ^{226}Th, ^{222}Th, and ^{216}Th isotopes which display an asymmetric to symmetric fission transition. This analysis has been performed within the HFB approach with (Q_{20}, Q_{30}, Q_{40}) as collective variable constraints, using the D1ST2a Gogny+tensor term interaction and comparing to the standard D1S Gogny interaction results. The effects from the tensor term on the potential energy surface landscape, and especially on barrier heights and its topology by opening a new valley in agreement with experimental data, are found to be crucial in the description of exotic actinide fission. We conclude that a tensor term should be integrated to the long range part of the effective interaction for a better description of the fission.

I. INTRODUCTION

The fission of the nucleus into two or more fragments is one of the most complex phenomenon in nuclear physics. Its complete modeling requires the knowledge of both static and dynamic properties of the fissioning system, namely, the static nuclear configurations out of equilibrium, the coupling between collective and intrinsic degrees of freedom, and the dynamics of large amplitude collective motion. Along the years, different types of approaches and models have been developed to tackle this difficult problem. Among them, fully microscopic approaches allow a description of the entire process from the initial configuration up to the scission point and beyond [1–20]. Even though this very ambitious program is far from being completed to date, it offers the possibility to take into account, in a unified and coherent way, both collective and internal degrees of freedom (and its interaction) along the fission path within a fully quantum-mechanical description of the time-dependent evolution of the fissioning nucleus. These approaches are based on a mean field description and therefore have to rely on the properties of effective nucleon-nucleon interactions, whose parameters are the only inputs of the model. Those parameters are fixed *a priori* once and for all using some fitting protocol which may or may not include fission data for a relevant set of nuclei.

In the past, most of the progress made in the field of the microscopic description of fission was accomplished essentially through a better understanding of the nuclear effective force. The first completely microscopic calculation was performed by the Orsay group with an early parametrization of the Skyrme interaction [21,22]. They calculated the symmetric fission barrier in ^{240}Pu within the HF+BCS approach under a constraint on the mass quadrupole moment. Even though the structure of the double-hump fission path was correctly described, the heights of the barriers were too high as compared to the experimental data extracted from measurements of neutron induced cross-sections. This was a common feature of many microscopic calculations carried out with different Skyrme parametrizations and for various actinides [23,24]. The analysis made by Dutta *et al.* for several Skyrme forces led to the conclusion that the second barrier height scaled like the value of the surface coefficient a_s of the interactions [25]. Similar studies were done with the original D1 Gogny force [3,4,26–29]. The results displayed similar features as the ones obtained with the Skyrme interactions, at very large deformations. To improve the agreement with experiment for the fission barriers of the typical benchmark nucleus ^{240}Pu, the surface tension coefficient of the D1 force was decreased leading to the well-known D1S parametrization [3,4,30]. Most of the properties of the D1S parametrization are similar to the ones of D1 but the barrier heights are in general in a much better agreement with the experimental ones. Another consequence of the fit was a desired weaker pairing strength in D1S with the corresponding impact on the collective inertias [31]. This is a direct consequence of the dependence of the inertias with the inverse of the pairing gap [32–34]. Once the static deformation and pairing properties of the force were fixed, it was conceivable to think on how to

*remi.bernard@anu.edu.au
†nathalie.pillet@cea.fr

improve the treatment of the dynamics of the fission process. A dynamical treatment using the time-dependent generator coordinate method plus the gaussian overlap approximation with the Gogny interaction was proposed in the '80s [3,4,30], with additional refinements thereafter [5,6,9,10,12,16,35,36]. The Gogny force in its various incarnations has been used not only in fission, but also in the rather successful description of many low energy nuclear properties at the mean field and beyond (see Refs. [37,38] for recent reviews).

In the early versions of the Skyrme and Gogny effective forces the tensor force, similar to the one in the one pion exchange potential, was disregarded to simplify calculations. Recently, this term has received renewed attention in connection with properties of both spherical and deformed nuclei described with the Skyrme interaction [39,40]. In the case of the Gogny interaction, a few attempts tackled this issue. One cites the pioneer work of Ref. [41] where only the like-particle component of the tensor force was included. The aim of the introduction of the tensor term was to improve the evolution of spherical single-particle states along isotopic chains. A full refitting of the Gogny force was carried out. However, no attention was paid to the pairing properties. The perturbative addition of a complete, long range tensor term proposed by Anguiano *et al.* [42–46] is a fully meaningful work in the case of the Gogny force. Indeed, the Gogny force was partly adjusted on the results obtained from a G-matrix plus second-order corrections [47,48], leaving room for reasonable extensions of the mean-field to treat explicitly the nuclear long-range correlations [49,50]. The main result obtained by Maire and Gogny, using the soft and local GPT effective force, was that the second-order corrections coming from the tensor force mostly affected the $(S = 1, T = 0)$ channel. In the construction of the effective Gogny force, most of the effect of the tensor force was taken into account in the strength of the density-dependent central term which also acts in the $(S = 1, T = 0)$ channel. Thus, the parameters of the standard Gogny interaction already take into account in a phenomenological way most of the effect of the tensor and, as a consequence, only a residual tensor with a long range is needed to fully take into account the effect of this part of the nuclear force. This results strongly softens the conclusions reached in the context of Skyrme interactions concerning the necessity to fully readjust the parameters of the interaction and the inadequacy of a perturbative addition of a tensor term. Of course, a complete refitting of all the parameters of the Gogny force would be highly desirable and this is an objective to be pursued in the short term. However, the present perturbative tensor allows one to look for new experimental data sensitive to the physics of a residual tensor term to constrain the additional parameters introduced. The study presented in this paper has been done in the same spirit.

To our knowledge, the impact of the tensor term in the potential energy surface and collective inertia required for fission has never been investigated. However, the role played by the tensor term has been investigated recently in several fusion studies [51–55]. The tensor interaction rearranges the position of the single particle orbitals changing the shell effects responsible for many of the properties of the quantities relevant to fission. In fact, it could be the missing ingredient

required to explain a symmetric bimodal fission mode recently found in some neutron-deficient thorium isotopes [56–59]. Recent experimental data provided by the experiments of the SOFIA collaboration have revealed the existence of such a symmetric bimodal mode, composed of the standard super-long mode and a new compact mode. This latter is characterized by a nonambiguous decrease of the mean value of the total prompt neutron multiplicity along the asymmetric to symmetric fission transition in the neutron-deficient thorium isotopes. In the present article, we discussed the role of the tensor interaction in the context of the Gogny force for the description of this new compact mode, using a Hartree-Fock-Bogoliubov approach (HFB) with several constraints. In particular, the role as collective variables of the Q_{20}, Q_{30}, and Q_{40} axially symmetric multipole moments is investigated.

The article is organized as follows. In Sec. II, the ingredients of the model used in the present study are discussed: The HFB method with constraints is briefly summarized and the D1ST2a parameterization of the Gogny interaction is described. This parameterization is an extension of D1S in which a perturbative tensor term is added. In Sec. III A, symmetric and asymmetric fission paths are shown for the $^{216-232}$Th isotopes. In this first analysis, the Q_{20} and Q_{30} collective variables are considered. The impact of the tensor term on the first and second barrier heights is discussed. In Sec. III B, the role of the Q_{40} multipole moment is highlighted and an explanation of the origin of the new compact symmetric fission mode is proposed. In Sec. III C, the various contributions of the D1S and D1ST2a interactions to the HFB binding energies are detailed. In Sec. III D, the distribution of the available energy at scission is discussed and evaluated to obtain general trends concerning the number of emitted neutrons in the case of the super-long and the compact mode. Finally, in Sec. IV, conclusions and perspectives are given.

II. STATIC MICROSCOPIC MODEL

A. Hartree-Fock-Bogoliubov method with constraints

As it is widely recognized, the mean-field and its extensions are powerful approaches to describe the wave function of the ground and excited states of the nucleus. However, fission is a time dependent phenomenon and a couple of extensions to the traditional stationary mean field are of use in its study: One is the time-dependent Hartree-Fock-Bogoliubov (TDHFB) method, which is the standard time-dependent generalization of the Hartree-Fock-Bogoliubov method, and the other is the time-dependent generator coordinate method (TDGCM), which is a fully quantum mechanics procedure. In both cases, the determination of the potential energy surface (PES), i.e., the HFB energy as a function of several relevant constraints is essential in determining the dynamics of the system and a lot of information can be gained by studying its evolution with the relevant degrees of freedom. In this paper, we have restricted ourselves to the study of the PES as a function of axially symmetric multipole variables to understand the impact of the tensor term. A full dynamical study in the framework of the TDHFB [60] or TDGCM will be the subject of future studies. Both approaches have their

own advantages and drawbacks. The TDGCM, which has been developed within the Gaussian Overlap Approximation (GOA), contains two main steps [2]

(1) a static calculation which determines the PESs and collective inertia, using the HFB method under constraints on relevant collective variables. The only ingredient is the nuclear effective interaction.

(2) a dynamic calculation in collective space and based on the previously determined input which describes the time evolution of the system up to the scission.

With this method one can obtain, for example, the fission fragment yield distributions. However, there is still room for improvement within the TDGCM+GOA framework, and one can mention the following improvements

(1) Remove some of the approximations used to compute the inertias, eventually using the exact ones [9],
(2) Include intrinsic excitation [2,10] to describe dissipation,
(3) Restoration of broken symmetries, like angular momentum or particle number [36],
(4) Removal of the GOA,
(5) Exploration of alternative effective interactions.

In the present work, we will pursue the issue of studying additional terms in the interaction, and for simplicity, we will restrict ourselves to the static part of the calculation. With this in mind we have analyzed the influence of the tensor term on the PES topology.

The HFB equation has been solved by conserving the axial, time-reversal and simplex symmetries. The parity has been broken to study the asymmetric fission through nonzero odd multipole moment paths. Moreover, two types of constraints have been considered: the first one concerns the average conservation of proton and neutron numbers, the second one is dedicated to multipole moments. Thus, the minimization principle on the total energy of the system reads

$$\delta \langle \Phi | \hat{H} - \lambda_n \hat{Q}_n - \lambda_p \hat{Q}_p - \sum_i \lambda_i \hat{Q}_{i0} | \Phi \rangle = 0, \qquad (1)$$

where $\hat{H}$ is the nuclear Hamiltonian, $\hat{Q}_n$ and $\hat{Q}_p$ the particle number operators, and $\hat{Q}_{i0}$ the multipole moment operators defined as

$$\hat{Q}_{i0} = \sqrt{\frac{4\pi}{2i+1}} \sum_{l=1}^{A} r_l^i Y_{i0}(\theta_l, \phi_l). \qquad (2)$$

The set of $\{\lambda_i\}$ are the Lagrange parameters associated with the corresponding constraint operators. The ith order multipole moment variable q_{i0} is defined as the average of the ith order multipole operator Q_{i0} in the HFB state $|\Phi\rangle$. The monopole moment q_{10} is set to zero to avoid contamination with spurious solutions coming from the breaking of the spatial translation symmetry. In the following, the one-dimensional (1D) fission paths are calculated using only the quadrupole moment variable as collective degree of freedom in addition to q_{10}. The symmetric path will refer to HFB calculations where q_{i0} are set to 0 fm^i for odd i, $i > 1$ whereas these latter are let free for the asymmetric path. Besides,

the two-dimensional (2D) fission PES are obtained with two constrained multipole moments, for example, $\{Q_{20}, Q_{30}\}$ or $\{Q_{20}, Q_{40}\}$. As for the 1D path, when the symmetric fission is studied, the q_{i0} are set to 0 fm^i for odd i.

We have implemented the tensor term in a computer code, named HFBaxialT [61], which is built upon the HFBaxial code [62], and uses an expansion of the quasiparticle operators in a harmonic oscillator basis to solve the HFB equation. In the HFBaxialT code the approximate second-order gradient method is employed to minimize the HFB energy [63]. The main advantage of this over other traditional iterative methods is the easy handling of constraints and an almost perfect rate of sucess in reaching a converged HFB solution.

The quasiparticle operators are expanded in an axially symmetric harmonic oscillator basis with a maximum value of quanta in the perpendicular direction $N_\perp = 2n_\perp + |m|$ of 14 and a maximum value of quanta in the z direction n_z of 21. Although the basis size is rather limited for the calculation of absolute values, it is enough for the calculation of relative effects, like energy differences (see below). The two oscillator lengths of the basis $b_\perp$ and b_z have been optimized as to minimize the HFB energy for each constrained calculation. The HFB solutions are computed from sphericity up to scission within a mesh defined by the step-size 2 b, 4 b$^{3/2}$, and 5 b^2 along the quadrupole, octupole, and hexadecapole moment variables, respectively.

B. The D1ST2a Gogny+tensor interaction

The present study has been done in the context of the Gogny interaction. As discussed in the introduction, the HFB mean-field obtained from the D1S Gogny interaction, which is historically known as the reference Gogny interaction to performed fission studies, takes into account in a phenomenological way most of the effect of the tensor term through its $(S = 1, T = 0)$ zero-range, density-dependent central term component. However, the effect of the long range part of a residual tensor is still missing and expected to play a role in specific situations, as, for example, an accurate description of the spin-orbit splittings, the un-natural parity states, the proton-neutron pairing or deformation properties.

The D1ST2a interaction is characterized by the adding of a perturbative tensor with long range and a weak strength to the Gogny D1S interaction [42–46]. Its analytical form reads as

$$V^{\text{D1TS2a}}(\vec{r}) = \sum_{i=1}^{2} \left(W_i + B_i P_{12}^\sigma + H_i P_{12}^\tau + M_i P_{12}^\sigma P_{12}^\tau \right) e^{-\vec{r}^2/\mu_i^2}$$
$$+ t_0 \left(1 + x_0 P_{12}^\sigma \right) \rho^\alpha(\vec{r}) \delta(\vec{r})$$
$$+ W_{LS} \overleftarrow{\nabla} \delta(\vec{r}) \wedge \overrightarrow{\nabla} . (\vec{\sigma}_1 . \vec{\sigma}_2)$$
$$+ \left(V_{\text{T1}} + V_{\text{T2}} P_{12}^\tau \right) \hat{S}_{12}(\vec{r}) e^{-\vec{r}^2/\mu_{\text{TS}}^2}, \qquad (3)$$

where the first three components correspond to the Gogny interaction with the D1S parametrization. In the above expression, the P_{12}^σ and P_{12}^τ operators are the traditional spin and isospin exchange operators, respectively. The set of parameters $\{W_i, B_i, H_i, M_i, i = 1, 2\}$, t_0, and W_{LS} are the coefficients of central, density-dependent central and spin-orbit terms. The

$\{\mu_i, i = 1, 2\}$ are the ranges of the Gaussian form factor and the coefficient x_0 is set to one to prevent the contribution of the density-dependent term to the proton and neutron pairing channels. Finally, $\vec{\sigma}$ is the three-dimensional spin operator and the operator $\hat{S}_{12}(\vec{r})$ is the usual tensor operator which is defined as

$$\hat{S}_{12}(\vec{r}) = 3 \frac{\vec{\sigma_1} \cdot \vec{r} \; \vec{\sigma_2} \cdot \vec{r}}{r^2} - \vec{\sigma_1} \cdot \vec{\sigma_2}. \tag{4}$$

The parameters of the nontensor terms of D1ST2a are the same as the D1S parameters. However, the parameters V_{T1} and V_{T2} of the tensor term are adjusted to reproduce the neutron single particle energies $1f_{5/2}$ and $1f_{7/2}$ in ^{48}Ca. The range $\mu_{TS} = \mu_2 = 1.2$ fm in the Gaussian form factor of the tensor has been chosen equal to the longest range of the two Gaussians in the central potential. We consider only the contribution of the tensor term to the mean field part of the HFB method whereas its contribution to the pairing channel is not taken into account. Therefore, and as in the D1S case, the only term contributing to the pairing channel in D1ST2a is the central potential. The reason for this omission is that the residual tensor term is not expected to play a relevant role in the proton and neutron pairings, unlike the proton-neutron one. Besides, the Coulomb exchange term of the HFB Hamiltonian is computed with the Slater approximation in the two cases.

Since in this study we are mainly interested in the impact of the tensor term in the fission process, special attention is paid to the total binding energy difference between the results obtained with the D1S and the D1ST2a interactions. To justify our choice of harmonic oscillator basis size, we have checked $\Delta(N_{sh}) = E_{HFB}^{Nsh}(D1S) - E_{HFB}^{Nsh}(D1ST2a)$ is the same for $N_{sh} = 14$ and $N_{sh} = 15$. Here N_{sh} is the maximum number of quanta in the perpendicular direction and it is consider as the equivalent of the number of shells in an spherical basis. The maximum values of n_z in the two cases are 21 and 23, respectively. The energy difference

$$\Delta E = |\Delta(15) - \Delta(14)| \tag{5}$$

has been calculated along the symmetric path of ^{226}Th. It averages 23 keV along the whole fission path and reaches 104 keV at large deformation which is still negligible compared to energy differences between the D1S and D1ST2a fission paths presented below.

The interplay between the D1ST2a tensor term and the quadrupole deformation properties was recently studied on various isotopic chains especially in the *sd*-shell [46]. However, typical quadrupole deformation values are much lower than the extreme ones encountered during the fission process. The results of this first study lead to the conclusion that, depending on the filling of the shells, the tensor term may strongly influence the HFB total energy, modify the potential energy landscape, and change the ground-state deformation. Pairing properties are also affected, especially a weakening of the particle number fluctuations is observed. An interpretation of such an influence in terms of spin-isospin contributions to the HFB energy has been given: Most of the time, the tensor term gives rise to a repulsive dominant proton-neutron contribution to the HFB energy. Attractive like-particle

contribution become dominant when the filling of the valence shells are in a spin-saturated/spin-unsaturated configuration, which happens around sphericity. As a logical continuation of this latter study, the present investigation is of prime interest as fission properties are strongly sensitive to PES landscapes in terms of collective variables and pairing degree of freedom.

III. RESULTS AND DISCUSSION

There are many observables that are required to fully characterize and understand fission. One can cite, for example, the mass and charge distribution of the fragments, the total kinetic energy (TKE), and the average neutron multiplicities $\langle \nu \rangle$.

The pioneer experiments of Schmidt at GSI Darmstadt based on the production of an exotic secondary beam by fragmentation of a primary beam of ^{238}U at relativistic energies, followed by Coulomb excitation of the secondary beam [64] opened up the door to the measurement of the charge distribution of the fragments in neutron-deficient actinides and pre-actinides. The isotopes ^{205,206}At, $^{204-209}$Rn, $^{206-212,217,218}$Fr, $^{209-219}$Ra, $^{212-226}$Ac, $^{217-229}$Th, $^{224-232}$Pa, and $^{230-234}$U were considered in a series of experiments. The results pointed out to a transition from asymmetric to symmetric fission in this region of the nuclear chart. However, the TKE measured in the $^{210-215,217-219}$Ra, $^{215-223}$Ac, $^{221-229}$Th, $^{226-232}$Pa, and $^{232-234}$U isotopes were known with low accuracy. Both the masses of the fragments and the average neutron multiplicity were not accessible in this kind of experiments. Starting from the same reaction mechanism but using a much more advanced experimental setup, the SOFIA experiments at GSI Darmstadt now allow one to obtain both charge and mass fission yields with an accuracy smaller than a mass unit as well as the average neutron multiplicity $\langle \nu \rangle$ [56,57]. Other techniques have been developed in parallel to study the fission of exotic nuclei. An example is the β-delayed fission process used at ISOLDE to study the fission of the very exotic nucleus ^{180}Hg which surprisingly shows asymmetric fission [65]. Another example are the transfer and fusion reactions using a beam of ^{238}U at 6 MeV per nucleon on a ^{12}C target used in the GANIL laboratory along with the VAMOS spectrometer [66].

The study of the fission of the neutron-deficient thorium isotopes, which are analyzed in this paper, has been motivated by the experimental data obtained during the 2012 SOFIA campaign at GSI Darmstadt [58,59]. The measurements concern the thorium isotopes ^{230}Th, ^{229}Th, ^{226}Th, ^{225}Th, ^{223}Th, ^{222}Th, and ^{221}Th. The experimental results confirm the asymmetric to symmetric transition in the mass distribution of the fragments already observed in Ref. [64]. In addition, they suggest the existence of a new bimodal symmetric fission mode in this region, composed of the standard super-long mode plus a new compact one. The compact component is experimentally characterized by the strong decrease of the average neutron multiplicity along the isotopic chain for decreasing neutron number.

A. Symmetric and asymmetric fission paths using Q_{20} and Q_{30} as collective variables

In this section, we analyze two fission paths, the symmetric and the asymmetric one, the latter being obtained by
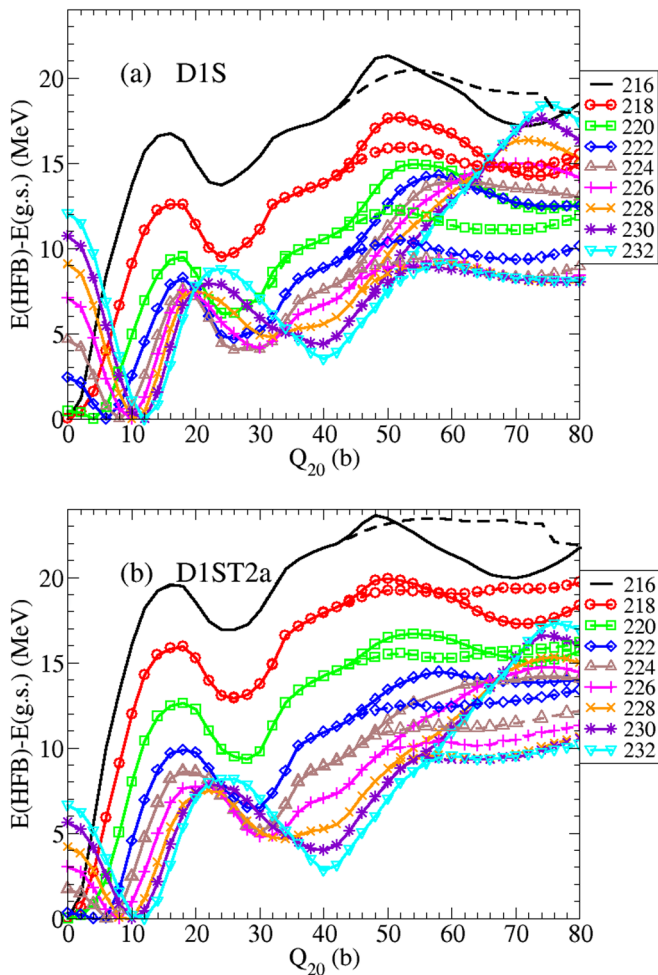
FIG. 1. Barrier heights of ^{216}Th up to ^{232}Th even-even isotopes for the symmetric (full lines) and asymmetric (dashed lines) paths, calculated at the HFB level with the D1S (top) and D1ST2a (bottom) Gogny interactions. Energies are expressed in MeV.

minimizing the total HFB energy for a nonzero average value of Q_{30}. In a first step, the global 1D axial deformation properties of the even-even $^{216-232}$Th isotopes are discussed. In a second step, the $\{Q_{20}, Q_{30}\}$ PESs are analyzed for the ^{216}Th, ^{222}Th, ^{226}Th, and ^{230}Th isotopes.

1. Global axial deformation properties of the even-even $^{216-232}$Th

The evolution of the HFB total energy calculated with the D1S (D1ST2a) Gogny force is shown up to the second barrier in Fig. 1(a) [Fig. 1(b)] for even-even thorium isotopes with the mass A ranging from 216 to 232. The symmetric paths are represented by the full lines and the asymmetric ones by the dashed lines. To facilitate the comparison the HFB ground-state binding energy has been subtracted for each isotopes.

Concerning the symmetric path, one observes large variations in the position of the minima and the maxima of the potential energy curves (PEC) and the barrier heights. By looking at the results obtained with the D1S Gogny force for the symmetric path [see Fig. 1(a)], one sees that the heaviest isotope, namely, ^{232}Th, is a well-deformed nucleus in its HFB

ground state is characterized by $Q_{20} \simeq 12$ b an energy gain of ~ 12 MeV with respect to the spherical configuration. The maximum of the first hump is obtained at $Q_{20} \simeq 24$ b and its height is ~ 9 MeV. The second well (fission isomer) is located around $Q_{20} \simeq 40$ b and is 3.5 MeV higher in energy than the HFB ground state. At $Q_{20} \simeq 74$ b, one encounters the second hump whose height is ~ 18 MeV.

By exploring the isotopic chain from ^{232}Th to ^{216}Th, one observes that the first well is continuously less and less deformed, the deformation energy decrease, in such a way that in ^{218}Th and ^{216}Th the HFB ground state is spherical. This effect is driven by the $N = 126$ neutron shell which corresponds to the ^{216}Th isotope. New experimental data have shown this shell closure effect at $N = 126$ in Po, Rn, Ra, and Th isotopes, with a relaxation in the U ones [67,68]. Calculations of the excitation energy of the 2_1^+ states (the first excited state in this nuclei) using the five-dimensional collective lead to the same conclusion, even though the relaxation effect is not so visible for U isotopes [69,70]. The clear increase of the energy of the 2_1^+ states signs this shell effect, the increase of the rigidity of the nuclei at $N = 126$, which is accompanied by an absence of neutron pairing energy at the minima of the potential energy surfaces. The heights of the first hump slightly decrease from ^{232}Th to ^{224}Th and increase again from ^{222}Th to ^{216}Th in such a way that it reaches ~ 17 MeV in the ^{216}Th isotope. The lightest isotopes are predicted to be more rigid than the other ones.

Concerning the second wells, one obtains the same trend as the one observed for the ground-state wells. The decrease of the associated Q_{20} value results in two deformation regions typical of the ^{216}Th isotope around 25 b and the ^{232}Th isotope around 40 b. The associated excitation energies are roughly the same from ^{230}Th to ^{222}Th and start to increase in a significant way in ^{220}Th, ^{218}Th, and ^{216}Th isotopes.

Finally, for the second hump, one notes that its quadrupole deformation is essentially distributed around two deformation regimes, namely, $Q_{20} \simeq 70$ b for ^{232}Th up to ^{226}Th isotopes, and $Q_{20} \simeq 50$ b for the lighter ones. The effect of the $N = 126$ neutron magic number seems to manifest again at these deformations. The heights of the second hump decrease from ^{232}Th to ^{224}Th isotopes, then start to increase up to the ^{216}Th one for which it is equal to 22 MeV. Most of the isotopes seems to display a third symmetric hump, as it was observed experimentally in the heavier isotopes ^{232}Th, ^{231}Th, and ^{230}Th [71–75].

From Fig. 1(b), one observes that the general trends obtained with the D1S Gogny interaction are still valid with the D1ST2a interaction. However, the ground-state deformation energies are found to be in general much smaller when the tensor term is taken into account. The main consequence is that a spherical HFB ground state is already obtained for ^{220}Th. Also, the tensor term is able to modify in a non-negligible way the height of the first and second humps, by increasing or decreasing them by several MeV depending on the isotopes. This last point, already visible by comparing Figs. 1(a) and 1(b), will be discussed further down.

Concerning the asymmetric path, one notes the following features with the D1S Gogny interaction. In the ^{232}Th isotope, the asymmetric path starts to be favorable in energy around $Q_{20} \simeq 50$ b, after the bottom of the second well. The height of

TABLE I. Energy differences $\Delta E = E^{\mathrm{D1ST2a}} - E^{\mathrm{D1S}}$ in MeV for HFB, mean field, and pairing energies. The tensor contribution to the D1ST2a HFB energy is also given.

Spher.	^{216}Th	^{222}Th	^{226}Th	^{230}Th	^{236}U	^{240}Pu
ΔE_{HFB}	4.310	3.713	3.279	2.881	1.557	1.922
ΔE_{MF}	−6.286	−6.213	−6.311	−6.433	−11.230	−6.517
ΔE_{pair}	8.056	7.564	7.393	7.310	12.780	7.396
E_{TS}	2.541	2.362	2.198	2.003	0.007	1.043

the second hump which corresponds to the asymmetric path is equal to $\simeq 9.3$ MeV. This value has to be compared to the symmetric one which is $\simeq 18.8$ MeV. As a general rule, the height of the asymmetric second hump is always lower in energy than the one of the symmetric second hump. Along the isotopic chain, one observes that the opening of the asymmetric valley occurs earlier and earlier in deformation and stabilizes in the ^{218}Th and ^{216}Th isotopes around $Q_{20} \simeq 42$ b. Moreover, the difference between the heights of the symmetric and the asymmetric second humps decreases continuously and regularly, when going towards the lightest isotopes. In the ^{216}Th isotope, it is equal to $\simeq 1.5$ MeV. For comparison, in the transitional nucleus ^{222}Th, it reaches $\simeq 4$ MeV.

With the D1ST2a Gogny interaction, the same observations can be done concerning the opening of the asymmetric valley. One notes the increase of the first and second humps in the lightest isotopes. The main difference comes from the effect of the tensor on the relative position of the maxima of the symmetric and asymmetric second humps, which is reduced considerably. For comparison with the D1S interaction, it is equal to $\simeq 7.5$ MeV in the ^{232}Th isotope and $\simeq 1.5$ MeV in the ^{222}Th isotope. In the ^{216}Th isotope, this difference tends to zero. Then, one concludes that the tensor term of the D1ST2a interaction tend to equate the heights of the symmetric and asymmetric second humps, rendering the symmetric path energetically competitive in the lightest thorium isotopes.

We turn now our attention to the various contributions to the total HFB energy, namely, the mean-field without the tensor (E_{MF}), the pairing (E_{pair}) and the tensor (E_{TS}) ones. In view of that, we have defined the three quantities ΔE_{HFB}, ΔE_{MF}, and ΔE_{pair} which represent the difference between the total HFB energies, the mean-field energies, pairing energies, respectively, calculated with the D1ST2a and the D1S interactions.

$$\Delta E_{\mathrm{HFB}} = E_{\mathrm{HFB}}^{\mathrm{D1ST2a}} - E_{\mathrm{HFB}}^{\mathrm{D1S}},$$
$$\Delta E_{\mathrm{MF}} = E_{\mathrm{MF}}^{\mathrm{D1ST2a}} - E_{\mathrm{MF}}^{\mathrm{D1S}}, \qquad (6)$$
$$\Delta E_{\mathrm{pair}} = E_{\mathrm{pair}}^{\mathrm{D1ST2a}} - E_{\mathrm{pair}}^{\mathrm{D1S}}.$$

TABLE III. Same as Table I but for the first-barrier configuration.

First barrier	^{216}Th	^{222}Th	^{226}Th	^{230}Th	^{236}U	^{240}Pu
ΔE_{HFB}	7.272	7.474	7.568	7.888	7.425	7.141
ΔE_{MF}	1.456	2.221	−1.422	5.365	4.596	3.440
ΔE_{pair}	0.293	−0.577	2.341	−3.574	−2.903	−1.824
E_{TS}	5.522	5.830	6.649	6.098	5.732	5.525

In addition, we have also considered E_{TS} which is the tensor contribution obtained with the D1ST2a interaction. Results are shown in Tables I–IV for the spherical and the ground state, the first hump, and the second well of ^{216}Th, ^{222}Th, ^{226}Th, and ^{230}Th, respectively. Values are also given for standard actinides, namely, ^{236}U and ^{240}Pu. All the thorium isotopes and ^{240}Pu shells are unsaturated at the Fermi levels. The case of ^{236}U is different as the proton $1h$ valence shell is spin saturated.

For the spherical configuration, one observes that ΔE_{HFB} is systematically positive. The same conclusion emerges when inspecting the ground-state configurations as well as the first hump and the second well configurations. These nuclei are predicted less bound with the D1ST2a interaction by several MeV, which indicates that the proton-neutron part of the tensor term is the source of the global effect. The analysis of the variation of ΔE_{MF} at the spherical point shows that it is systematically negative, which points out to a Hartree-Fock type mean-field which is more bound with the D1ST2a interaction by several MeV. This can be explained by the shifting of a few single-particle orbitals in presence of the tensor term around the Fermi level. This shifting produces a variation of the pairing energies ΔE_{pair} which is, in turn, systematically positive and larger in absolute value. As the pairing strength is identical for both interactions, one deduces that the rearrangement of the single-particle spectrum in presence of the tensor term tends to reduce the pairing contribution for spherical configurations in these nuclei. Finally, E_{TS} is found positive. One notes the almost zero value obtained for ^{236}U which is spin saturated in protons.

At the ground-state deformation, which are prolate for five nuclei (^{216}Th is excluded as its ground state is spherical), the detailed analysis of ΔE_{HFB} leads to opposite observations for ΔE_{MF} and ΔE_{pair}. The mean-field is less bound with the D1ST2a interaction but the pairing energy is stronger. The contribution of the tensor term E_{TS} is always positive and larger than the one obtained at the spherical point.

At the deformations of the first hump, the variation ΔE_{HFB} is essentially dominated by the contribution E_{TS}. Both the

TABLE II. Same as Table I but for the ground-state configuration.

g.s.	^{216}Th	^{222}Th	^{226}Th	^{230}Th	^{236}U	^{240}Pu
ΔE_{HFB}	4.310	5.843	7.336	7.968	8.667	8.782
ΔE_{MF}	−6.286	4.336	8.337	6.359	5.576	4.755
ΔE_{pair}	8.056	−1.941	−5.847	−3.947	−3.629	−3.016
E_{TS}	2.541	3.448	4.846	5.555	6.720	7.043

TABLE IV. Same as Table I but for the second-well configuration.

Second well	^{216}Th	^{222}Th	^{226}Th	^{230}Th	^{236}U	^{240}Pu
ΔE_{HFB}	7.537	7.638	7.982	7.572	7.977	7.852
ΔE_{MF}	1.976	4.455	5.448	1.884	1.645	−2.561
ΔE_{pair}	−0.335	−2.290	−3.387	−0.120	0.480	4.700
E_{TS}	5.895	5.472	5.920	5.807	5.852	5.713

quantities ΔE_{MF} and ΔE_{pair} have strongly decreased, in absolute value, in comparison with the two previous cases. No general trend is obtained for their signs as they depend on the nucleus.

At the deformations of the second well, the contribution E_{TS} takes rather similar value for the six nuclei and it is still large. For the thorium isotopes, ΔE_{MF} and ΔE_{pair} keep the same sign, associated with a less bound mean-field and stronger pairing correlations with the D1ST2a interaction. For ^{236}U, ΔE_{MF}, ΔE_{pair}, and E_{TS} are found positive for the D1ST2a interaction, which can be interpreted as a global repulsion. For ^{240}Pu, the tensor term induces a more bound mean-field and a decrease of the pairing correlations.

One concludes that, even though ΔE_{HFB} and E_{TS} are found systematically positive for the six nuclei in the four states considered (spherical, ground state, first hump, and second well), no general law emerges concerning the mean-field and the pairing contributions except for the fact that they have in general opposite sign. The results are subtle and depend strongly on the shell structure around the Fermi levels.

2. Symmetric and asymmetric fission paths in ^{230}Th, ^{226}Th, ^{222}Th, and ^{216}Th isotopes

After these global comments on the axial deformation properties with and without parity breaking in even-even $^{216-232}$Th isotopes, one details now the symmetric and the asymmetric paths up to scission with both full 2D $\{Q_{20}, Q_{30}\}$ potential energy surfaces (PES) and the associated 1D potential energy curves (PEC). Calculations have been done for the ^{230}Th, ^{226}Th, and ^{222}Th isotopes which sign experimentally the asymmetric to symmetric fission transition, as explained previously. We have kept also the ^{216}Th isotope because of its $N = 126$ magic neutron number even though not experimentally measured. Moreover, all along the paper, we have kept the pre-scission configurations in the considered collective variable space as far as possible in deformation and left aside the post-scission configurations which are characterized by the absence of matter between the two fragments, as it is usually done in fission studies (see, for example, Refs. [12,16]). In the following, the post-scission configurations will be grouped under the term "fusion valley."

On Fig. 2, the PES, obtained using the D1S Gogny interaction, for the four isotopes considered are plotted. The x-axis corresponds to the elongation Q_{20} which ranges between 30 b (around the deformation of the second well) and 200 b. The y axis represents the asymmetry Q_{30} which varies between $0\,\text{b}^{3/2}$ and $40\,\text{b}^{3/2}$. The color code ranges over 10 MeV for all the panels (a)–(d). It represents the energy difference between the HFB total binding energy for given values of Q_{20} and Q_{30}, and the lowest HFB value obtained in the existing PES. For convenience a Delaunay triangulation has been performed as in Ref. [76] for all the 2D PES. The results with the D1ST2a interaction are displayed in Fig. 3. The corresponding 1D asymmetric and symmetric paths are drawn in Figs. 4 and 5, respectively, according to the collective variable Q_{20} between 0 b and 250 b. The total HFB energy E_{HFB} has been renormalized to the ground-state total energy $E_{\text{g.s.}}$. Results are indicated for both the D1S (black full circles) and the D1ST2a

(red full squares) interactions. The evolution of the associated collective variables Q_{30} (for the parity breaking paths) and Q_{40} are shown on Figs. 6 and 7.

For the ^{230}Th isotope, Fig. 2(a), one observes the existence of an asymmetric path which starts around $Q_{20} \simeq 50$ b [see Fig. 6(a)] and leads to static HFB configurations with a large asymmetry. This path is clearly the lowest in energy. It seems to be rather flat (with a slight decrease of the energy for increasing Q_{20}) and displays scissionned configurations around $Q_{20} \simeq 137$b for $Q_{30} \simeq 40\,\text{b}^{3/2}$ and $Q_{40} \simeq 110\,\text{b}^2$, as seen from Fig. 4(a). From Figs. 3(a), 4(a), and 6(a), one concludes that these observations hold also for the D1ST2a interaction, except that the energy of this large asymmetry path increases slowly from the second hump up to the scissionned configuration.

For comparison, as seen from Figs. 2(a), 5(a), and 7(a), one obtains that the symmetric path is less favorable energetically because of the height of the second hump which is predicted to be $\simeq 18$ MeV ($\simeq 17$ MeV) for the D1S (D1ST2a) Gogny interaction. Moreover, one sees that the scissionned configuration, which defines in our case the exit point, is encountered at a much larger value of Q_{20}, around $\simeq 211$ b for D1S and $\simeq 229$ b for D1ST2a, with a larger hexadecapole moment equal to $Q_{40} \simeq 250\,\text{b}^2$ and $300\,\text{b}^2$, respectively.

For the ^{226}Th isotope, the path which leads to large asymmetry scission still exists with the D1S interaction, as seen in Fig. 2(b). It starts around $Q_{20} = 45$ b as indicated in Fig. 6(b). It presents a more pronounced third hump than in the ^{230}Th isotope, around $Q_{20} \simeq 105$ b and $Q_{30} \simeq 30\,\text{b}^{3/2}$, which is easily identifiable in Fig. 4(b). The tensor term tends to increase by $\simeq 1$ MeV the height of the second hump and the rest of the large asymmetry path displays a continuous increase of the total energy up to the scissionned point, as already discussed for the ^{230}Th isotope. The first scissionned configurations are obtained at $Q_{20} \simeq 140$ b with the D1S interaction and at a little smaller value for the D1ST2a interaction, namely, 132 b. Moreover, from Fig. 6(b), one sees that the values of Q_{30} and Q_{40} are very similar to the ones obtained at the exit point in the ^{230}Th isotope.

In any case, comparing Fig. 4(b) with Fig. 5(b), one observes that for both interactions, the asymmetric path is again lower in energy. Indeed, even though the height of the second hump for the symmetric path is ~15 MeV for both interactions, which is lower than the one in ^{230}Th isotope, it is still higher than the asymmetric one which is equal to ~9 MeV (10 MeV) for the D1S (D1ST2a) interaction. One adds that the symmetric exit points are characterized by very similar values than the ones obtained for the ^{230}Th isotope but with a little decrease of Q_{20}.

For the ^{222}Th isotope, the situation starts to be different. From Fig. 2(c), one observes that this big asymmetry path gets clogged, which was already the case in the ^{230}Th and ^{226}Th isotopes with the D1ST2a interaction. At some point, around $Q_{20} \simeq 90$ b, it is no longer energetically favorable. This corresponds to the energy discontinuity observed in the red full squares and black full circles curves, Fig. 4(c). Here, the blue full line and the green dashed line correspond to the continuation of paths which lead to large asymmetry scission and which are clearly higher in energy by several MeV. At
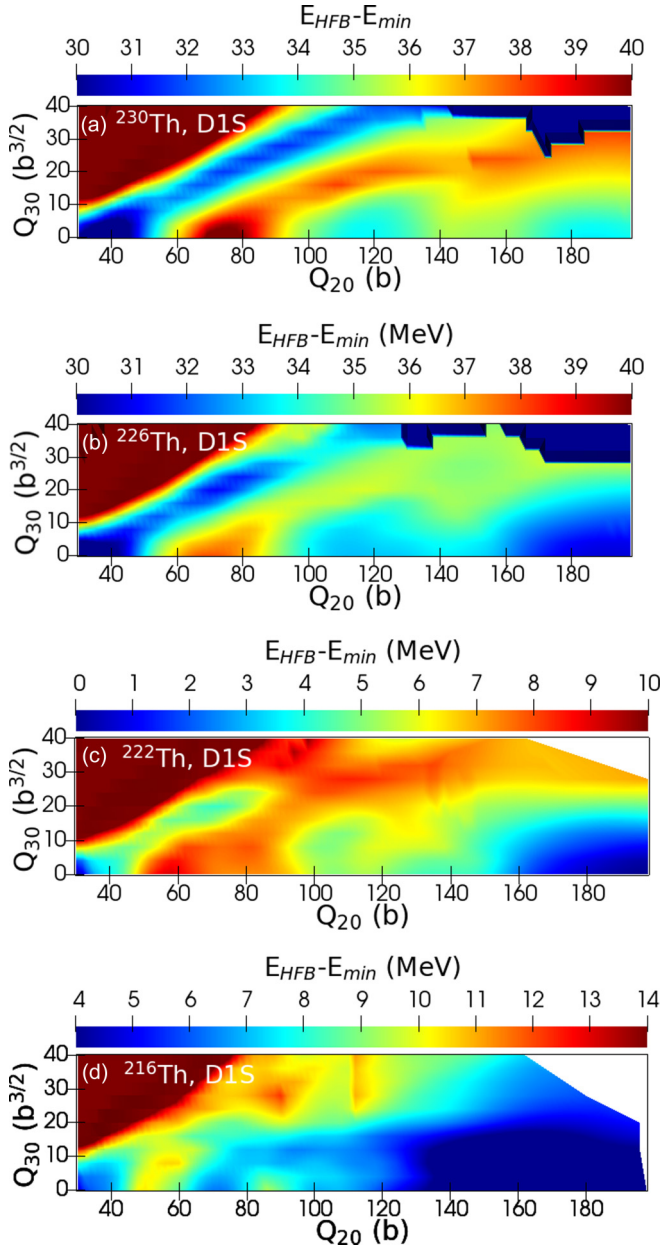
FIG. 2. PES's for (a) ^{230}Th (b) ^{226}Th (c) ^{222}Th, and (d) ^{216}Th as a function of the elongation Q_{20} in b and the mass asymmetry Q_{30} in $b^{3/2}$. The color code indicates the HFB total energy normalized to the lowest value of the PES and spans a range of 10 MeV. Calculations have been done with the D1S Gogny interaction.

FIG. 3. Same as described in the caption of Fig. 2 but for the D1ST2a Gogny interaction.

this deformation, it is higher by ∼1.5 MeV (3 MeV) with D1S (D1ST2a) interaction. The minimum energy principle implies a path with a smaller asymmetry around 13 $b^{3/2}$, which is located in a new local minimum as observed in Fig. 2(c). Elongating more and more the nucleus, one finds that the symmetric configuration is energetically favorable around $Q_{20} \simeq 120$ b, which is signaled by the energy discontinuity observed in Fig. 4(c) at this quadrupole deformation. The system continues along the symmetric path up to scission. The exit point appears at $Q_{20} \simeq 205$ b for both interactions, which is characteristic of the well-known super long symmetric
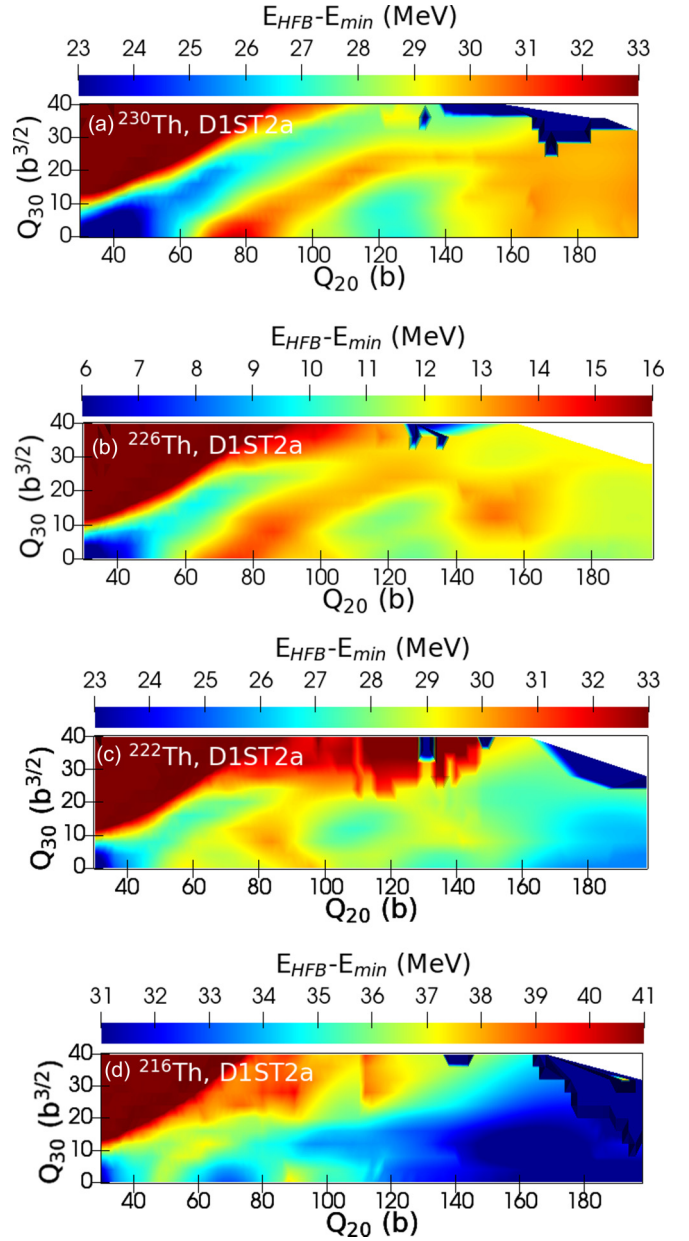
fission mode, with $Q_{40} \simeq 260$ b. At this level, no sign of possible compact fission can be highlighted. The most important phenomenon obtained in ^{222}Th isotope is the rebalancing of the heights of the symmetric and asymmetric second humps due to the tensor term, as seen from Figs. 4(c) and 5(c). This rebalancing is characterized by an increase of the height of the asymmetric second hump in presence of the tensor term, whereas the symmetric one is essentially unchanged. From a 1D energetic viewpoint, this renders the full symmetric path more probable (or less improbable!) when the tensor term is added, and therefore the symmetric fission mode.

For the ^{216}Th isotope, the same type of mixed asymmetric-symmetric path manifests as the one found in the ^{222}Th isotope [see Figs. 2(d), 3(d), 4(d), 5(d), 6(d), and 7(d)]. One
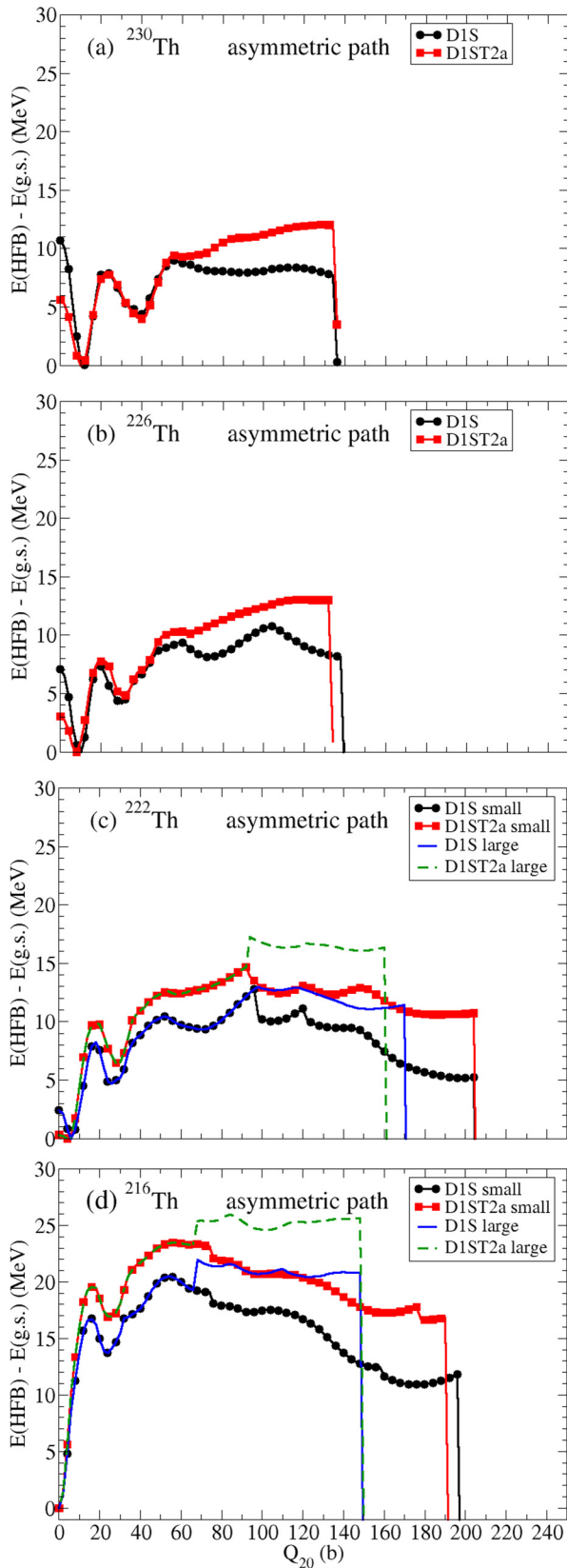
FIG. 4. Asymmetric fission paths in (a) ^{230}Th, (b) ^{226}Th, (c) ^{222}Th, and (d) ^{216}Th isotopes calculated with the HFB approximation. Results correspond to D1S (full black circles) and D1ST2a (full red squares) Gogny interactions. The blue and the green curves are the large asymmetry path for the D1S and the D1ST2a interactions. See text for explanations. Energies are expressed in MeV.
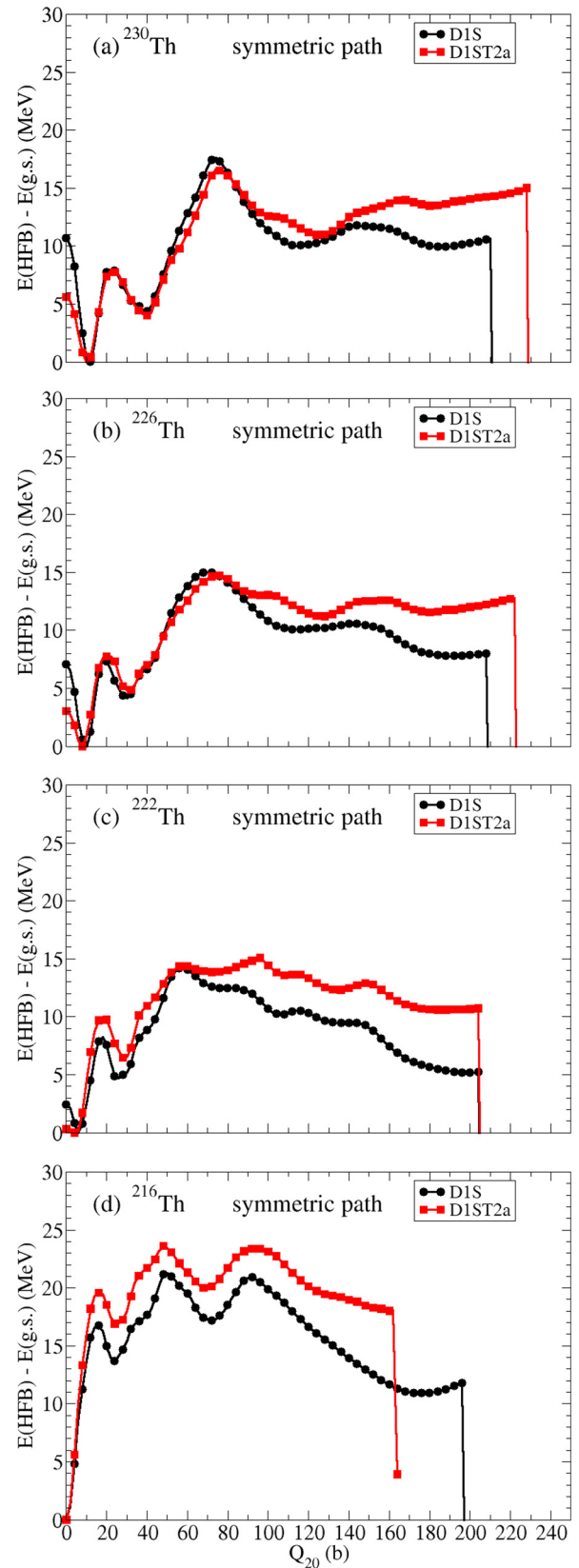
FIG. 5. Symmetric fission paths in (a) ^{230}Th, (b) ^{226}Th, (c) ^{222}Th, and (d) ^{216}Th isotopes calculated with the HFB approximation. Results correspond to the D1S (circles) and D1ST2a (squares) Gogny interactions. Energies are expressed in MeV.
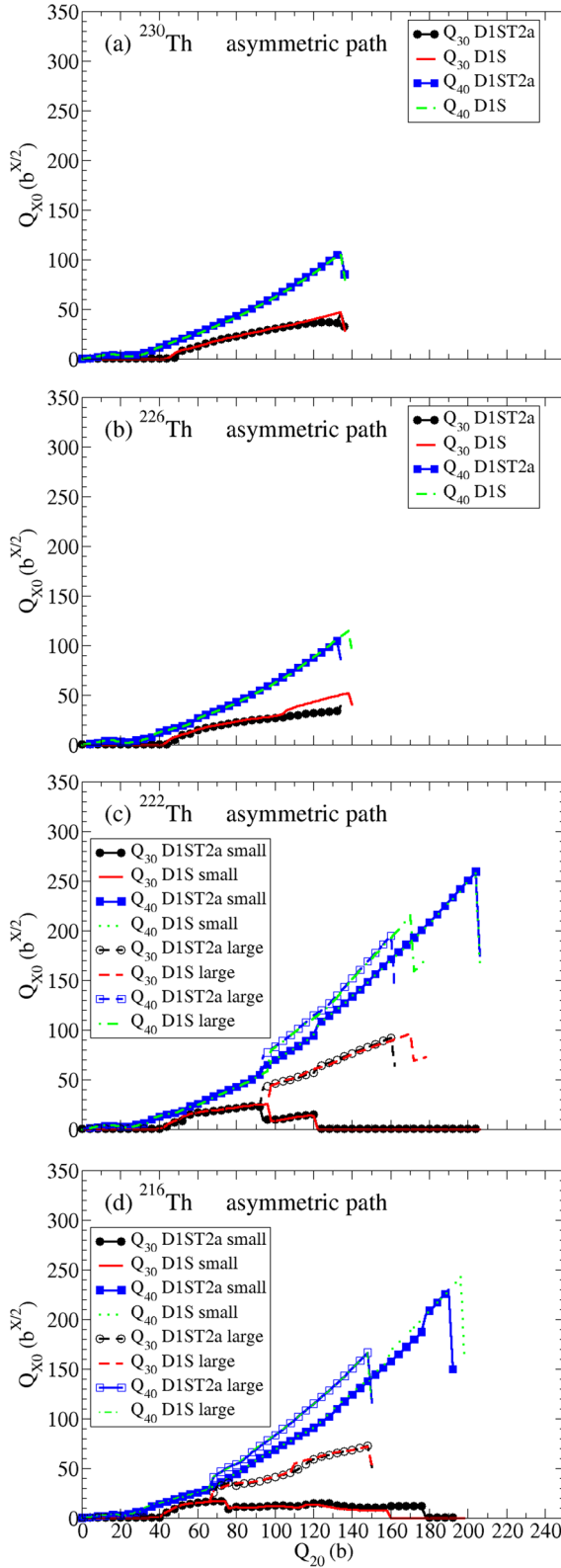
FIG. 6. Evolution of Q_{30} and Q_{40} collective variables along the asymmetric path in (a) ^{230}Th, (b) ^{226}Th, (c) ^{222}Th, and (d) ^{216}Th isotopes calculated with the HFB approximation. Results are provided for both the D1ST2a and the D1S Gogny interactions. When they exist, the results for the small and the large asymmetry paths are shown.
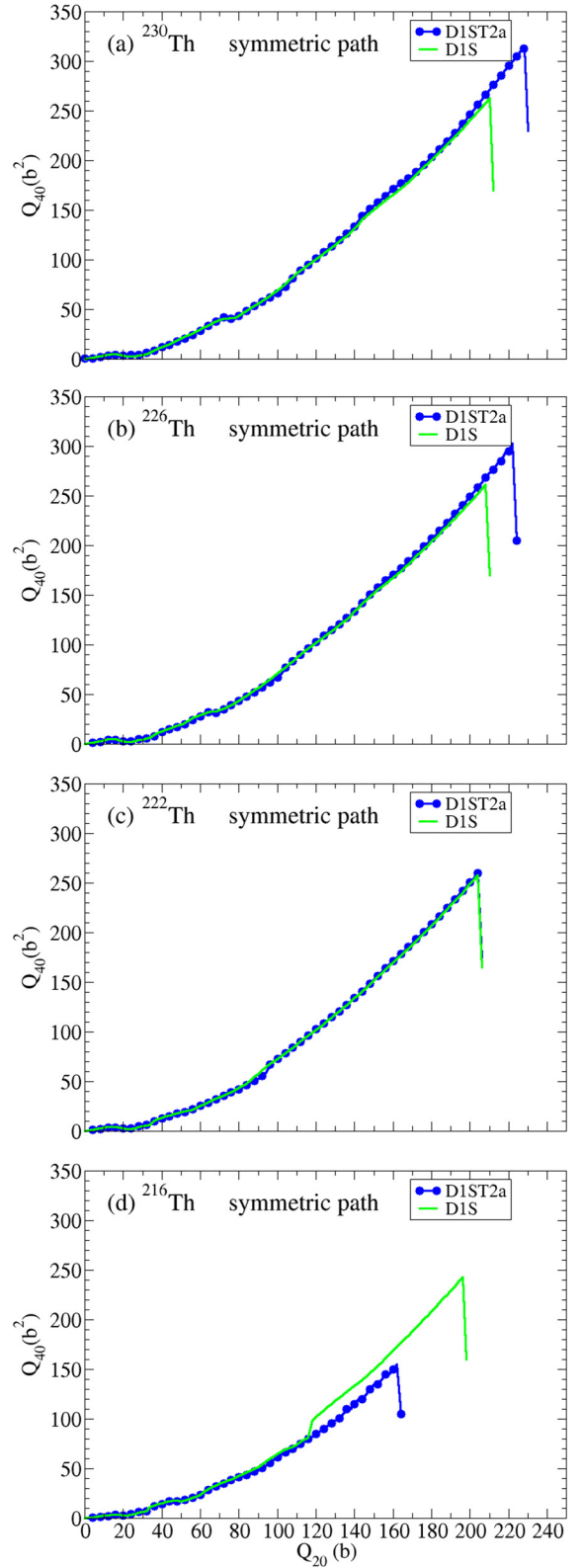
FIG. 7. Evolution of Q_{40} collective variable symmetric path in (a) ^{230}Th, (b) ^{226}Th, (c) ^{222}Th, and (d) ^{216}Th isotopes calculated with the HFB approximation. Results are provided for both the D1ST2a and the D1S Gogny interactions.

obtains first a path which leads to large asymmetry scission from $Q_{20} \simeq 40$ b up to $Q_{20} \simeq 75$ b, then a path with small asymmetry characterized by $Q_{30} \simeq 10$ b$^{3/2}$ up to $Q_{20} \simeq 160$ b (178b) with the D1S (D1ST2a) interaction, followed by a symmetric path. In that case, the first symmetric scissionned point is obtained at $Q_{20} \simeq 198$ b for the D1S interaction, and a smaller value of 191 b for the D1ST2a one. Now, looking at the pure symmetric path [Fig. 5(d)], one observes that, in the case of the D1ST2a interaction, the exit point is obtained at $Q_{20} \simeq 162$ b which is different and much smaller than the value deduced from the mixed asymmetry path. This is an unusual short value for a symmetric scission, more characteristic of an asymmetric scission. As we will see later, this is a first theoretical hint of the existence of the compact fission mode that could be correlated with the observations of the SOFIA experiment [58,59]. From Fig. 7(d), one sees that this mode is characterized also by a much smaller value of the hexadecapole moment Q_{40} at the exit point, which is equal to ~ 150 b^2.

Finally, one observes a global and significant increase of the height of the barriers in the ^{216}Th isotope which has a neutron magic number equal to 126, for both the symmetric and the asymmetric paths, whatever the interaction. One notes that the symmetric second hump height is lower than the asymmetric one in the case of D1ST2a. In conclusion, one sees that the tensor term plays a nonnegligible role on the barrier height. Its behavior is a detailed one which acts differently on the symmetric and the asymmetric path. At this stage, within these 1D and 2D analysis made in terms of Q_{20}, Q_{30} collective variables, no clear explanation is available concerning its role in the existence of the symmetric compact fission mode along the isotopic chain. It appears only in the ^{216}Th isotope.

B. Tensor term effect and symmetric compact scission—Role of the Q_{40} collective variable

In this part, the potential role of the Q_{40} collective variable to explain the existence of the symmetric compact fission mode in light thorium isotopes is investigated. This possibility has been suggested by the results obtained for the symmetric path in the ^{216}Th isotope with the D1ST2a interaction, for which the first scissionned configuration is characterized by both a much smaller value of Q_{20} and Q_{40} in comparison with the other isotopes. To perform this analysis, the 2D PESs using the {Q_{20} and Q_{40}} collective variables, have been calculated with both interactions. The quadrupole moment Q_{20} ranges from 130 b up to 300 b and the hexadecapole one Q_{40} from 90 b$^{3/2}$ up to 300 b$^{3/2}$. The results are shown on Fig. 8 (Fig. 9) for the D1ST2a interaction (D1S) for the four selected thorium isotopes.

Concerning the ^{230}Th isotope, the calculation with D1ST2a shows a unique valley as can be seen in Fig. 8(a). On the right-hand side of this main valley, called V1 in the following, one notes the existence of a kind of small plateau colored in yellow and located a few MeV above the bottom of the valley V1. For comparison, in the case of the D1S interaction [see Fig. 9(a)], only a well-defined valley exists. The exit point is characterized by $Q_{20} \simeq 230$ b (210 b) and $Q_{40} \simeq 315$ b^2

(255 b^2) for the D1ST2a (D1S) interaction. To analyze in more details these results, the evolution of the barrier heights between the fission V1 and the fusion (called "fus") valleys as a function of Q_{20} is shown in Fig. 10(a) for both the D1ST2a (full black circles) and the D1S (full red squares) interactions. These barrier heights have been defined as the values deduced from transversal slices to the path which follows the bottom of the valley. At the beginning, around $Q_{20} \simeq 130$ b, the barrier height is around 7 MeV for the D1ST2a interaction. Then, increasing the elongation Q_{20} of the nucleus, it decreases and reaches a value which is lower than 1 MeV around 180 b. Finally, it remains stable up to $\simeq 225$ b and disappears around 230 b at the exit point. With the standard D1S interaction, the value of the barrier is systematically higher by 2–3 MeV along the symmetric path. Only at the end, its value decreases rapidly and goes to zero at a value of Q_{20} slightly smaller, around $\simeq 210$ b. From these results, we conclude that the tensor term tends to decrease by several MeV the height of the V1 to fusion barrier.

For the ^{226}Th isotope, the difference between the patterns obtained with the D1ST2a and the D1S interactions begins to intensify. The main valley V1 existing in the ^{230}Th isotope is still there. However, as seen from Fig. 8(b), the plateau changes into a kind of protovalley, called V2 in the following. It appears around $Q_{20} \simeq 140$ b for a smaller value of Q_{40} which characterizes the valley V1, around $\simeq 110$ b^2. The evolution of the values of the different transverse barrier heights is reported on Fig. 10(b). Concerning the principal valley V1, the barrier heights "V1 → fus" (full black circles for D1ST2a and full red squares for D1S) are of the same order of magnitude as the ones obtained in ^{230}Th, even a little smaller. Their relative behavior is similar with a cancellation of the barriers around $Q_{20} \simeq 222$ b for D1ST2a and $\simeq 208$ b for D1S. Concerning the barrier between the principal valley V1 and the protovalley V2 (green stars), which exists with the D1ST2a interaction and which is referred to as "V1 → V2," its height is equal to $\simeq 4$ MeV at its nascence around $Q_{20} \simeq 140$ b and decreases by 2 MeV up to $Q_{20} \simeq 157$ b where V2 suddenly disappears. At this elongation, the barrier between the principal valley V1 and the fusion valley "fus" is still ~ 2 MeV.

The value of the barrier between the protovalley V2 and the fusion valley, named "V2 → fus" (full blue triangles), starts at $\simeq 2.5$ MeV, decreases regularly and cancels around $Q_{20} \simeq 165$ b. Please note that its associated exit point is characterized by smaller values of Q_{20} and Q_{40} than the ones of the main valley V1, $\simeq 166$ b and $\simeq 150$ b^2, respectively. It signals the possible existence of a symmetric compact fission mode. The main question which remains to answer is the possibility of feeding the protovalley which is located at a couple of MeV above V1 in this isotope. One can invoke two possibilities in the adiabatic hypothesis: either by tunnel effect or by excitation of a transverse mode which is the most probable mechanism. Another possibility would be to populate the valley through individual quasi-particle excitation with the available energy acquired after the saddle point.

In the case of the ^{222}Th isotope, the observations made for ^{226}Th are confirmed. The protovalley transforms into a well-identified second valley which appears around $Q_{20} \simeq 130$ b and $Q_{40} \simeq 100$ b^2, as seen in Fig. 8(c). For comparison, the
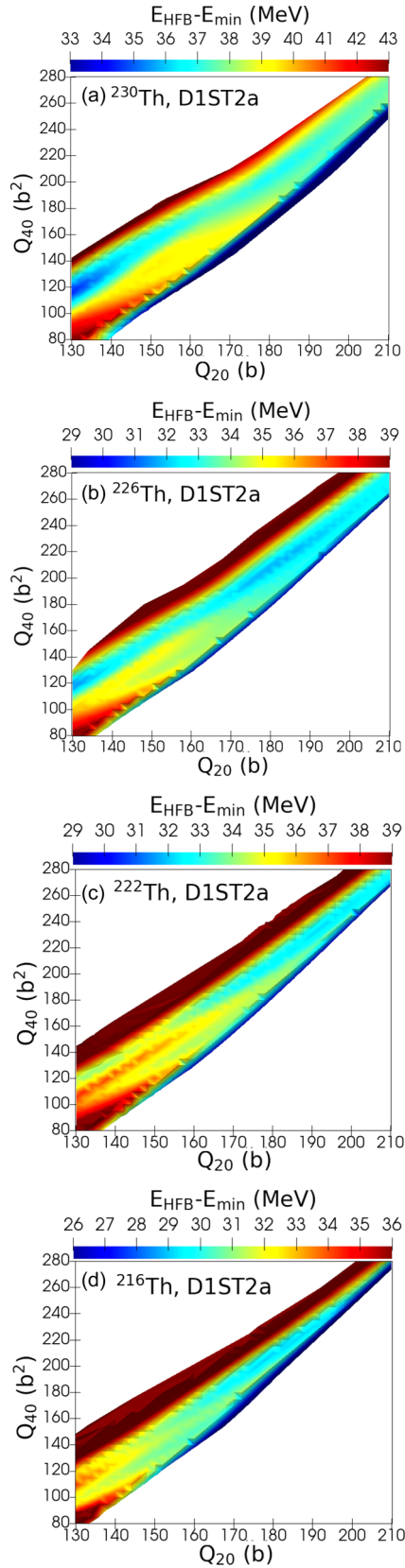
FIG. 8. $\{Q_{20}, Q_{40}\}$ potential energy surfaces associated with the symmetric fission path ($Q_{30} = 0$) for (a) ^{230}Th, (b) ^{226}Th, (c) ^{222}Th, and (d) ^{216}Th. Calculations have been done with the D1ST2a interaction. Energies are expressed in MeV.
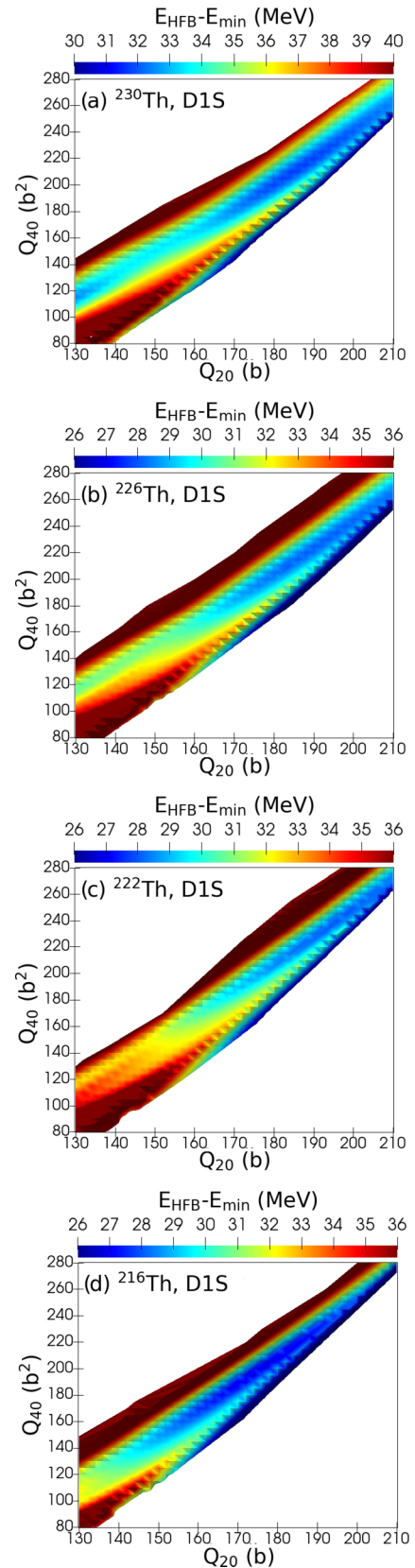
FIG. 9. Same as described in the caption of Fig. 8 but for the D1S interaction.
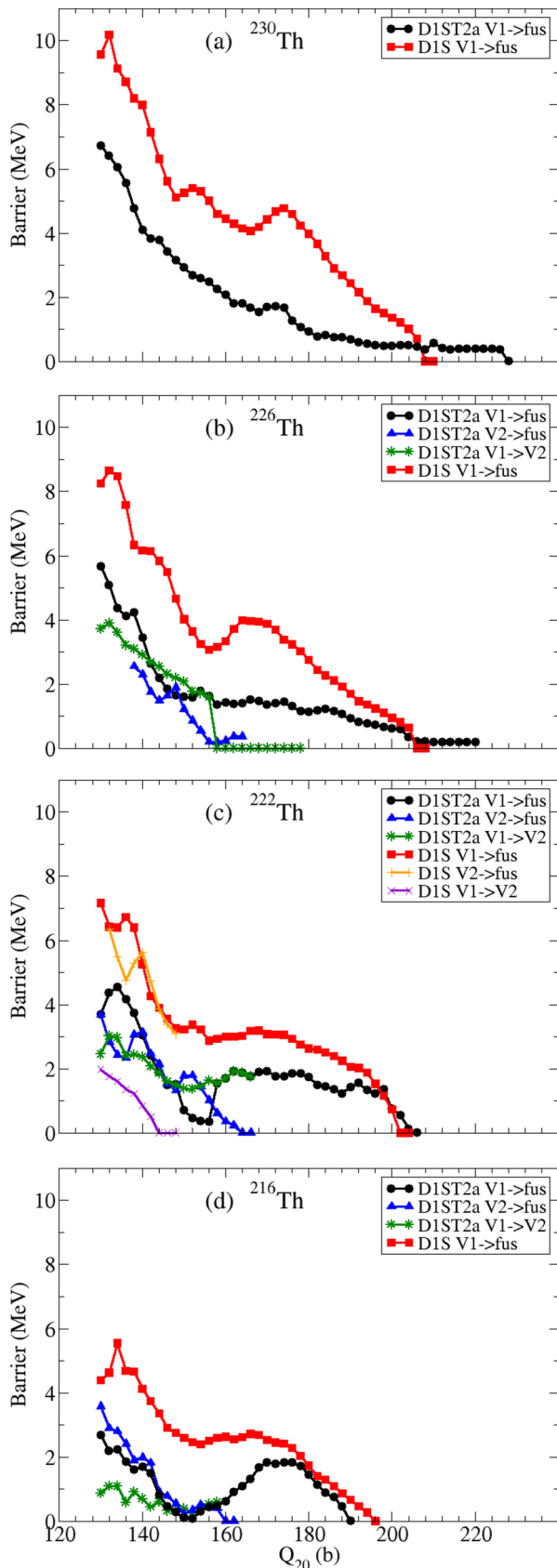
FIG. 10. Evolution of barrier heigths in (a) ^{230}Th, (b) ^{226}Th, (c) ^{222}Th, and (d) ^{216}Th calculated with the D1S and D1ST2a Gogny interactions. Energies are expressed in MeV.

associated value of Q_{40} for the V1 valley is $\simeq 120$ b^2, which corresponds to an increase of 20%. These values associated with the new valley V2 are also smaller than the ones of the protovalley in the ^{226}Th isotope. We note that the new valley V2 is higher in energy than the valley V1, but it is lower in energy than the protovalley V2 found in ^{226}Th isotope. Its exit point is found at $Q_{20} \simeq 166$ b and $Q_{40} \simeq 150$ b^2. The exit point of the principal valley V1 is characterized by $Q_{20} \simeq 208$ b and $Q_{40} \simeq 265$ b^2, which are much larger values. Thus, the V1 and V2 valleys define two distinct modes in the symmetric path for ^{222}Th: the classic super long mode from V1 and a new compact mode induced by the tensor term of the nuclear interaction.

For the D1S interaction, a kind of "tilted plateau" appears on the right side as can be seen in Fig. 9(c). It clearly ends in the principal valley V1. The structure of this "tilted plateau" seems to be different from the structure of a valley. In particular, it disappears in the ^{216}Th isotope, as discussed below. The exit point corresponds to a well-elongated fission with $Q_{20} \simeq 206$ b and $Q_{40} \simeq 255$ b^2. The evolution of the barrier heights can be seen on Fig. 10(c). Because of the existence of the "tilted plateau" with the D1S interaction, we have drawn for both interactions the barriers "V1$\to$ fus," "V2$\to$ fus," and "V1$\to$ V2," where V2 represents the second valley in the case of D1ST2a and the tilted plateau for D1S. Those barriers are the energy difference between the bottom of the first valley and the crest separating the two valleys.

When considering the "V1$\to$ fus" barrier obtained with the D1ST2a interaction (full black circles), one has to be careful with the interpretation and has also to consider the barrier "V1$\to$ V2" (full blue triangles) which separates both valleys. Indeed, the principal valley is not connected directly to the fusion valley at the beginning of the path up to the exit point of the valley V2. Around $Q_{20} \simeq 130$ b, the barrier height "V1$\to$ fus" is equal to $\simeq 4$ MeV, which is lower by 1.5 MeV in comparison with the one obtained in ^{226}Th. Then, it quickly decreases up to $Q_{20} \simeq 156$ b where it reaches a small value of $\simeq 400$ keV. However, as previously mentioned, the "V1$\to$ V2" barrier height in this deformation region is around 1.7 MeV. Moreover, around $Q_{20} \simeq 158$ b, both barriers "V1$\to$ V2" and "V1$\to$ fus" become mixed up. The "V1$\to$ V2" barrier disappears at $Q_{20} \simeq 168$ b (the exit point of the valley V2). Only the barrier "V1$\to$ fus" exists for larger values of Q_{20}. Its height stay more or less constant up to $Q_{20} \simeq 200$ b and is equal to $\simeq 1.7$ MeV. Then, it decreases rapidly and goes down to zero at $Q_{20} \simeq 208$ b. Finally, one observes that the "V1$\to$ V2" barrier height is not changing too much, being equal to $\simeq 3$ MeV for the smallest Q_{20} values and $\simeq 1.7$ MeV for larger ones. Concerning the "V2$\to$ fus" barrier height, after a fluctuation around $\simeq 3$ MeV for the smallest values of Q_{20}, it decreases and disappears at $Q_{20} \simeq 165$ b, a value compatible with the compact fission mode.

For the D1S interaction, the situation is different because of the presence of the tilted plateau. First of all, the height of the tilted plateau to the bottom of the principal valley V1, called "V1$\to$ V2," changes rapidly (purple crosses). Around $Q_{20} \simeq 130$ b, it is equal to $\simeq 2.0$ MeV. Around the elongation $Q_{20} \simeq 145$ b, it disappears. For larger deformations, the principal valley V1 is directly connected to the fusion valley

TABLE V. Values of the Q_{20} (expressed in b) and Q_{40} (expressed in b^2) collective variables of the exit points in the ^{230}Th, ^{226}Th, ^{222}Th, and ^{216}Th isotopes. Calculation have been done for the symmetric path with the D1S Gogny force.

Nucleus	Valley	Q_{20} (b)	Q_{40} (b^2)
^{230}Th	V1	210	255
^{226}Th	V1	208	255
^{222}Th	V1	206	255
^{216}Th	V1	198	240
	D1S, Symmetric path.		

(full red circles) through the barrier "V1$\rightarrow$ fus" whose height is $\simeq$3 MeV. Then, it begins to decrease and goes away at a larger deformation $Q_{20} \simeq 202$ b. The exit point of the principal valley V1 is obtained for $Q_{20} \simeq 206$ b and $Q_{40} \simeq 255\,b^2$.

In the ^{216}Th isotope, one obtains for the first time a valley V2 which is lower in energy than the principal valley V1 as can be observed in Fig. 8(d), when using the D1ST2a interaction. The exit point of the valley V2 is still strongly compatible with a compact fission mode, with $Q_{20} \simeq 162$ b and $Q_{40} \simeq 150b^2$. For the principal valley V1, the exit point has $Q_{20} \simeq 190$ b and $Q_{40} \simeq 225\,b^2$. In the calculations with the D1S interaction a unique valley V1, corresponding to a well-elongated fission mode, is obtained. This valley ends at $Q_{20} \simeq 198$ b and $Q_{40} \simeq 240\,b^2$.

Looking at the barrier heights in Fig. 10(d), one observes that all the barriers, namely, "V1$\rightarrow$ fus," "V2$\rightarrow$ fus," and "V1$\rightarrow$ V2," start with a lower energy than the equivalent ones obtained in the previous isotopes with either D1ST2a or D1S Gogny interaction. In particular, at $Q_{20} \simeq 130$ b, the "V2$\rightarrow$ fus" barrier (full blue triangles) is higher in energy than the "V1$\rightarrow$ fus" one. This is consistent with the fact that the principal valley V1 is located above the V2 one. This observation remains true up to $Q_{20} \simeq 158$ b where the valley V2 disappears. Here, the "V1$\rightarrow$ fus" barrier height starts to increase again and reaches $\simeq$2 MeV at $Q_{20} \simeq 172$ b. Then, it decreases and fades away at $Q_{20} \simeq 190$ b.

It is also interesting to note that the barrier "V1$\rightarrow$ V2" (green stars) is very low at the beginning of the curve, around $\simeq$1 MeV. Then, it decreases with the quadrupole deformation up to $Q_{20} \simeq 152$ b, where it reaches $\simeq$300 keV. It increases again up to $Q_{20} \simeq 158$ b where reaches the $\simeq$ 800 keV height

TABLE VI. Same as Table V but for the D1ST2a Gogny interaction.

Nucleus	Valley	Q_{20} (b)	Q_{40} (b^2)
^{230}Th	V1	230	315
^{226}Th	V1	222	295
	V2	**166**	150
^{222}Th	V1	208	265
	V2	**166**	150
^{216}Th	V1	190	225
	V2	**162**	150
	D1ST2a, Symmetric path.		

TABLE VII. Same as Table V but for the asymmetric valley.

Nucleus	Valley	Q_{20} (b)	Q_{30} ($b^{3/2}$)	Q_{40} (b^2)
^{230}Th	V1	136	28	80
^{226}Th	V1	140	40	94
^{222}Th	V1	172	69	159
^{216}Th	V1	150	52	116
	D1S, Asymmetric path.			

and disappears at the end of the valley V2. Finally, for the D1S interaction, the behavior of the "V1$\rightarrow$ fus" barrier is similar to the one obtained in the ^{222}Th isotope, but with a little shorter extension before disappearing.

All the characteristics of the exit points, in terms of values of the collective variables Q_{20}, Q_{30}, and Q_{40}, and associated with the symmetric and the asymmetric valleys, are given in Tables V–VIII, for both the D1S and the D1ST2a interactions.

Preliminaries calculations in neutron-deficient uranium and radium isotopes seem to display also a second symmetric valley corresponding to a compact fission mode.

To finish this section let us say a few words about the origin of the valleys V2 which are well pronounced in the ^{222}Th and ^{216}Th isotopes. In Fig. 11, a 2D representation of the symmetric $\{Q_{20}, Q_{40}\}$ PESs calculated with the D1ST2a interaction for both isotopes is displayed. Here, results include smaller values of Q_{20}, namely, $Q_{20} = 0$ b and beyond. Besides, we have kept the fusion valley which appears in dark blue on the right side of the fission valleys.

In Fig. 11(a) we observe the existence of a plateau in ^{222}Th which extends between $Q_{20} \simeq 90$ b and $\simeq$100 b. Just after the plateau, one sees the nascence of the valley V1. Concerning the valley V2, it appears at a much larger elongation, around $Q_{20} \simeq 128$ b. Invoking only the topology of the PES and this difference in quadrupole deformation, we can argue that, in the adiabatic approximation, the flux of the wave function will feed directly and largely the valley V1 in the region $Q_{20} \in$ [100b, 130b]. In addition, using the findings of the (Q_{20}, Q_{40}) dynamical study proposed by J.F. Berger and collaborators in the context of cold fission for the ^{240}Pu nucleus [4], the valley V2 may be fed partly by the wave function through the excitation of transverse modes for larger elongations. The height of the barrier "V1$\rightarrow$ V2" discussed previously [see Fig. 10(c), green stars] is fully compatible with such a process. In that context, the symmetric fission is understood as a mixing of a compact and the super long modes whose weight can be determined by a dynamical treatment.

TABLE VIII. Same as Table VI but for the asymmetric valley.

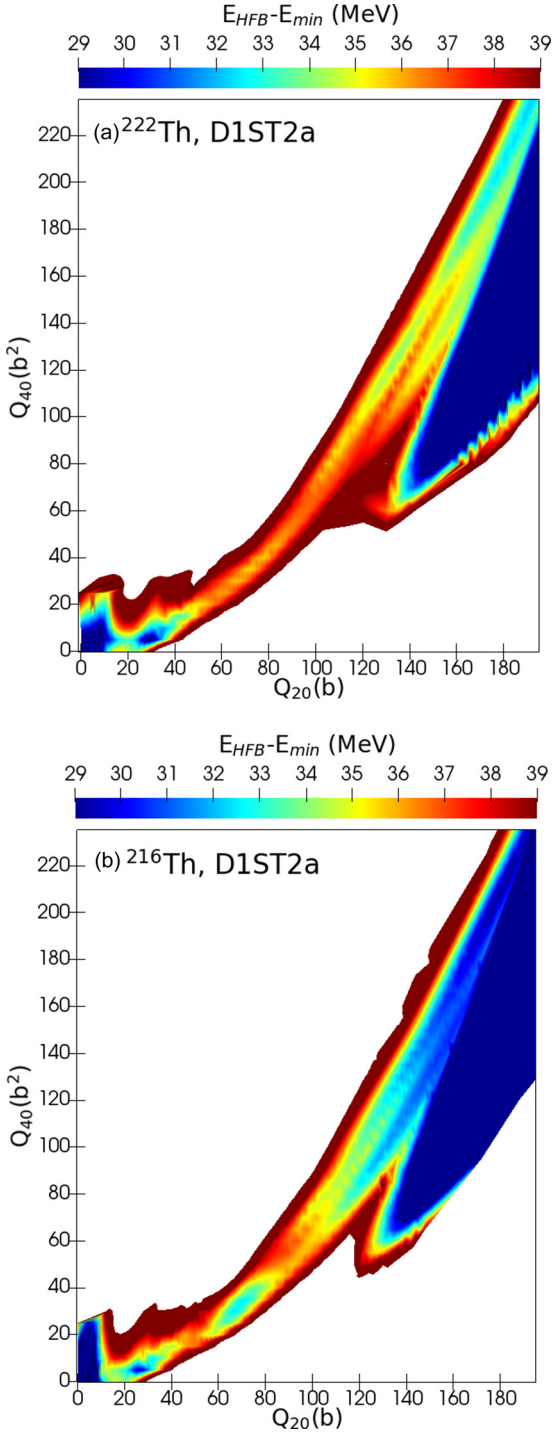| Nucleus	Valley	Q_{20} (b)	Q_{30} ($b^{3/2}$)	Q_{40} (b^2)
^{230}Th	V1	136	33	85
^{226}Th	V1	134	39	87
^{222}Th	V1	162	64	142
^{216}Th	V1	150	51	116
	D1ST2a, Asymmetric path.			

FIG. 11. Creation of the two valleys using Q_{20} and Q_{40} as collective variables along the symmetric path, in (a) ^{222}Th and (b) ^{216}Th with the D1ST2a interaction. Energies are expressed in MeV.

In ^{216}Th [Fig. 11(b)], the pattern is rather different. Indeed, the V2 valley appears first around $Q_{20} \simeq 110$ b and it is the lowest in energy. From the plateau in energy which exists between 88 b and 100 b and the lowest energy path which is located on the side of the lowest Q_{40} value, one concludes that, this time, the valley V2 will be the one preferentially fed by

the time evolution of the collective wave function. As in ^{222}Th and considering the heights of the barriers "V2→ fus" and "V1→ V2" [see Fig. 10(d), full blue triangles and green stars, respectively], one predicts an exchange between the valleys V2 and V1 through transverse modes and the manifestation of both the compact and super long symmetric modes.

C. Interplay between tensor force, deformation, and pairing correlations

We now turn our attention to the mechanism responsible for the existence of the new valley V2, which is interpreted as the experimentally observed new symmetric compact mode. The present analysis has been done by inspecting the different contributions to the total HFB energy. More precisely, we have separated the HFB binding energy in two (three) contributions in the case of the D1S (D1ST2a) interaction in such a way that

$$E_{\mathrm{HFB}}^{\mathrm{D1S}} = E_{\mathrm{MF}}^{\mathrm{D1S}} + E_{\mathrm{pair}}^{\mathrm{D1S}},$$
$$E_{\mathrm{HFB}}^{\mathrm{D1ST2a}} = E_{\mathrm{MF}}^{\mathrm{D1ST2a}} + E_{\mathrm{pair}}^{\mathrm{D1ST2a}} + E_{\mathrm{TS}}, \qquad (7)$$

where E_{MF} is the mean-field energy, not including the tensor contribution in the D1ST2a case. The particle-particle energy $E_{\mathrm{pair}} = \frac{1}{2}\mathrm{Tr}\,(\Delta\kappa)$ is usually referred to as the pairing energy and is proportional to the amount of pairing correlations in the system. It should not be confused with the real pairing correlation energy given by the difference between the HFB and HF energies. Finally, the tensor energy E_{TS} is the contribution of the tensor term to the HFB energy and therefore it is zero in the D1S case.

In Fig. 12, we display the energy differences:

$$\Delta E_{\mathrm{HFB}} = E_{\mathrm{HFB}}^{\mathrm{D1ST2a}} - E_{\mathrm{HFB}}^{\mathrm{D1S}} \quad \text{(full black circles)},$$
$$\Delta E_{\mathrm{MF}} = E_{\mathrm{MF}}^{\mathrm{D1ST2a}} - E_{\mathrm{MF}}^{\mathrm{D1S}} \quad \text{(full red squares)},$$
$$\Delta E_{\mathrm{pair}} = E_{\mathrm{pair}}^{\mathrm{D1ST2a}} - E_{\mathrm{pair}}^{\mathrm{D1S}} \quad \text{(full green triangles)},$$

as well as E_{TS} (blue stars), as a function of the hexadecapole moment Q_{40} expressed in b^2. We have also depicted the accumulated sum $S_{\mathrm{MF+pair}} = \Delta E_{\mathrm{MF}} + \Delta E_{\mathrm{pair}}$ (orange full diamonds). The calculations have been performed with the additional constraint $Q_{20} = 130$ b (left column), 140 b (central column), and 150 b (right column), for (a) ^{230}Th, (b) ^{226}Th, (c) ^{222}Th, and (d) ^{216}Th.

The most streaking feature observed in all the panels is the similar behaviour of ΔE_{HFB}, whatever the isotope and the deformation Q_{20}. Starting from the barrier which separates the fusion and the fission valleys at the smallest Q_{40} values, one first observes a linear increase of ΔE_{HFB}. The positive sign of this variation indicates that the D1ST2a interaction produces less binding energy than the D1S one. A maximum is obtained at a Q_{40} value which corresponds to the ridge between the new valley V2 (when it exists) and the main valley V1. One notes that, even if the valley V2 is not apparent, as it is the case in ^{230}Th, a maximum for E_{TS} is also obtained in the same Q_{40} region. In addition, the intensity of the phenomenon is nearly the same for all the isotopes. It starts around 3–4 MeV at the fusion-fission barrier with a variation of 3–4 MeV. After the maximum reached by E_{TS}, ΔE_{HFB} decreases or stabilizes in several cases.
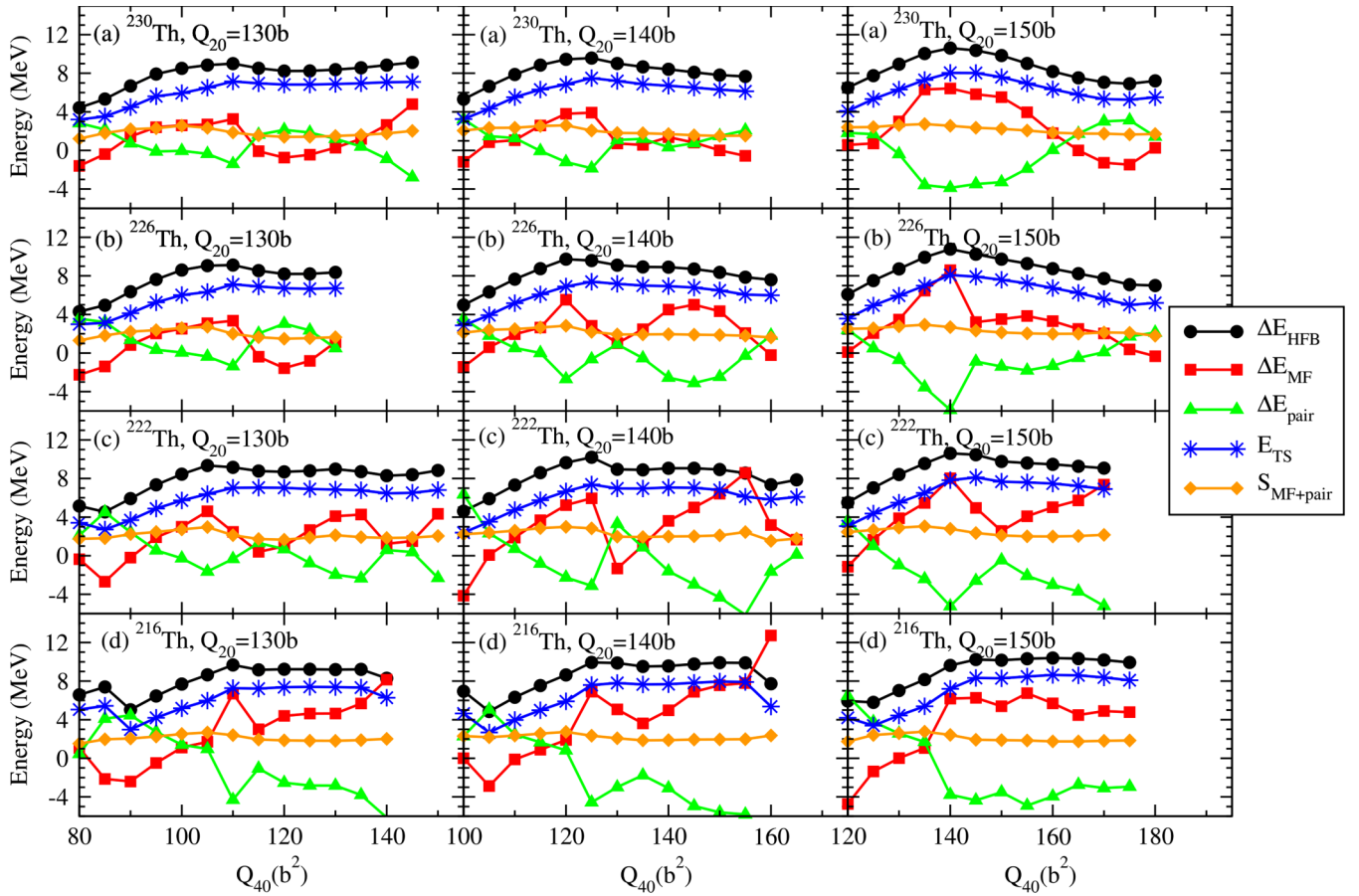
FIG. 12. Evolution of ΔE_{HFB}, ΔE_{MF}, ΔE_{pair}, and E_{TS} (see text for explanation) as a function of Q_{40} (in b^2) for (a) ^{230}Th, (b) ^{226}Th, (c) ^{222}Th, and (d) ^{216}Th. Calculations have been done at $Q_{20} = 130$ b (left column), 140 b (central column), and 150 b (right column). Energies are expressed in MeV.

The general trend obtained for ΔE_{HFB} seems to be strongly correlated with the E_{TS} contribution and this represents a first strong hint of a tensor effect. To better isolate this effect, we have plotted in Fig. 13 the evolution of $E_{HFB} - E_{HFB}$ (g.s.) as a function of Q_{40}, calculated with D1S (full black circles) and D1ST2a (full red squares). In the same figure, the curve corresponding to the results obtained with the D1ST2a force but subtracting the tensor energy E_{TS} (full orange diamonds) is also shown. To facilitate the interpretation of the results, the quantity E_{TS} (blue stars) is also drawn. As an illustration, calculations are shown for the four isotopes with the constraint $Q_{20} = 140$ b. The similarity of the "D1S" and "D1ST2a-E_{TS}" curves leads to the conclusion that the birth of the new valley V2 is due to the increase of E_{TS} with the hexadecapole moment up to a certain value of Q_{40} which is coupled to the decreasing slope of the MF plus pairing contributions obtained in this region. This effect is not sufficient in ^{230}Th to create a new valley V2. However, the slope of the curve is softened by the tensor contribution (see the curves with red square and orange diamonds). The preservation of the valley V1 for larger values of Q_{40} is due to the decrease or stabilization of E_{TS}. One notes that in ^{222}Th there is a local effect around $Q_{40} \simeq 135 b^2$ for the "D1ST2a-E_{TS}" curve which leads to a more pronounced minimum than for the "D1S" curve. To end with the effect associated with the

E_{TS} contribution, we have displayed in Fig. 14 the evolution of the proton E_{TSp} (full red squares) and the neutron E_{TSn} (full blue triangles) component of the total tensor energy E_{TS} (black full circles) as a function of Q_{40}, for all the considered isotopes. We observe that in the region of the new valley, both proton and neutron contributions increase with the proton one dominating over the neutrons. For larger values of Q_{40}, they show a rather constant behavior with similar contributions in the two cases.

The mean-field E_{MF} and the pairing E_{pair} energy contributions depicted in Fig. 12 suffer from strong variations when the tensor term is added to the D1S interaction. They vary out of phase with changes of sign for both contributions. When the mean-field is less bound with the D1ST2a interaction ($\Delta E_{MF} \geqslant 0$), the pairing correlations increase and vice versa.

The sum of the two quantities has a positive value as can be seen in the curve $S_{MF+pair}$. Besides, the behavior of the quantity is found to be rather constant (the variations are within less than 1 MeV). This last result confirms the role played by the tensor energy E_{TS} in the creation of the new valley, which was discussed previously.

We would like to end this part by discussing the pairing contribution. Indeed, even though from a total energy perspective the role of the pairing seems to be washed out by the mean field contribution, many observables are sensitive
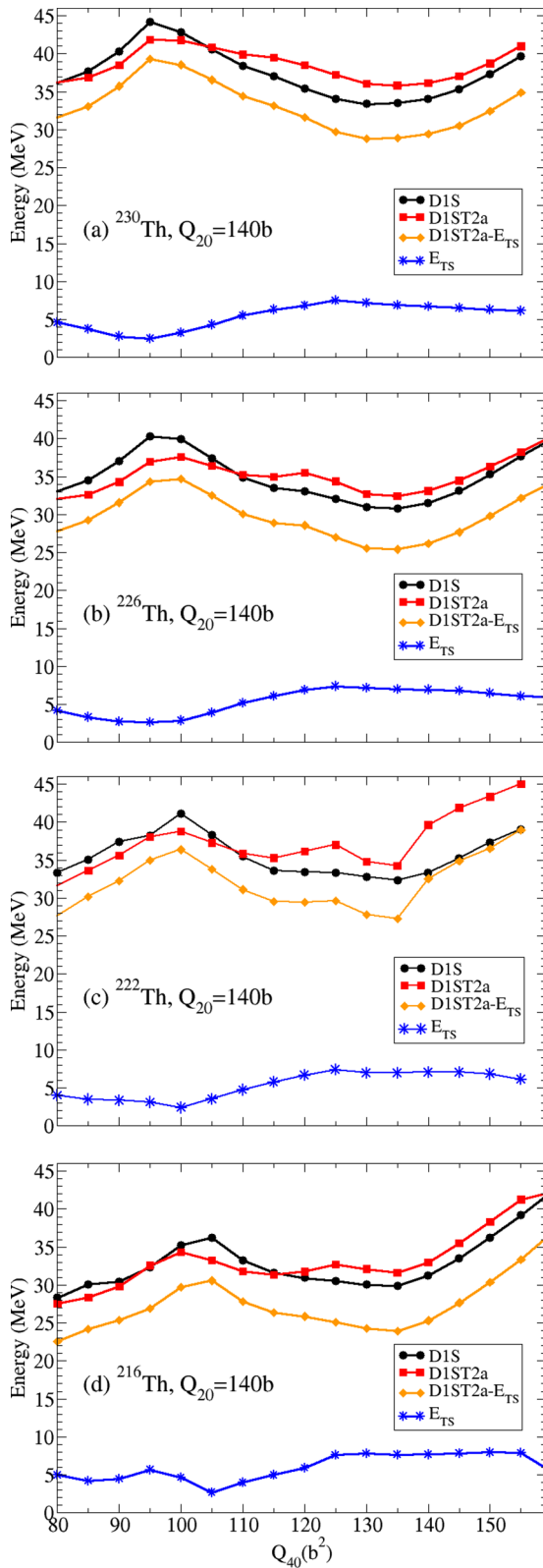
FIG. 13. Evolution of E_{HFB}-E_{HFB} (g.s.) as a function of Q_{40} calculated with D1S (black full circles) and D1ST2a (red full squares). Moreover, we have drawn the curve corresponding to adding the tensor energy E_{TS} to the D1S energy (orange full diamonds). For comparison, the tensor contribution E_{TS} (blue stars) is also depicted. Energies are expressed in MeV.
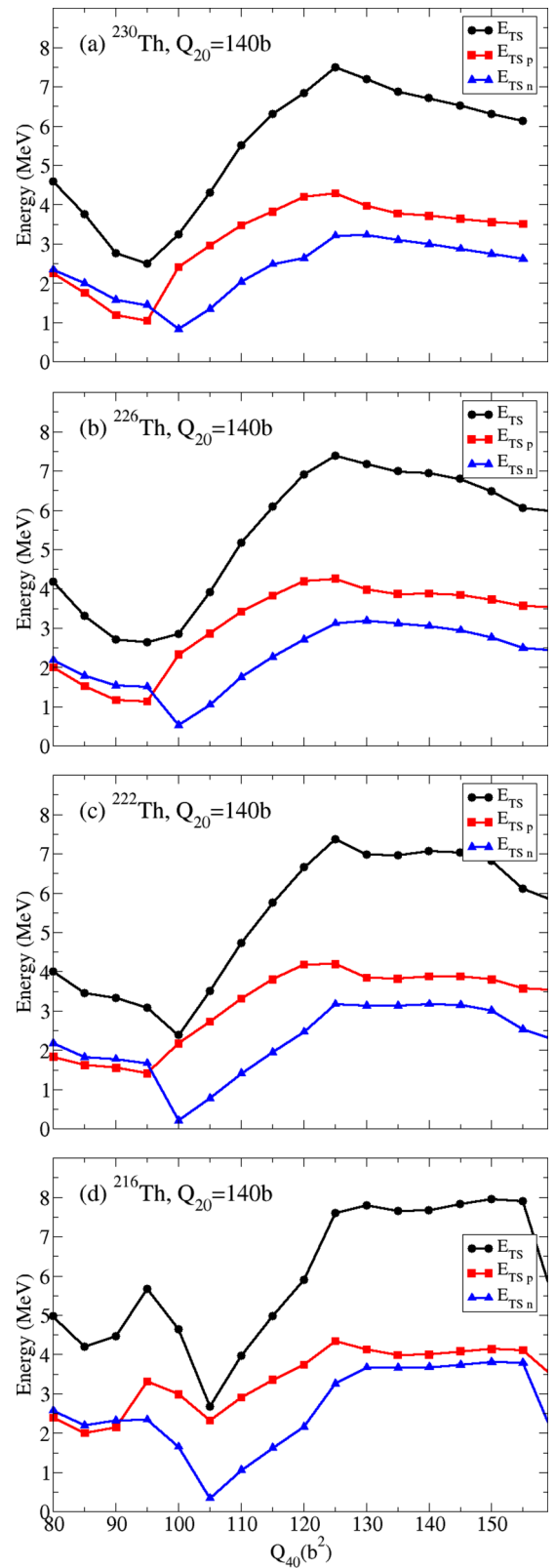
FIG. 14. Evolution of the total tensor energy E_{TS} (black full circles), its proton component E_{TSp} (red full squares) and its neutron component E_{TSn} (blue full triangles) as a function of Q_{40} (expressed in b^2) at $Q_{20} = 130$ b. See the text for details. Calculations have been done for (a) ^{230}Th, (b) ^{226}Th, (c) ^{222}Th, and (d) ^{216}Th. Energies are expressed in MeV.
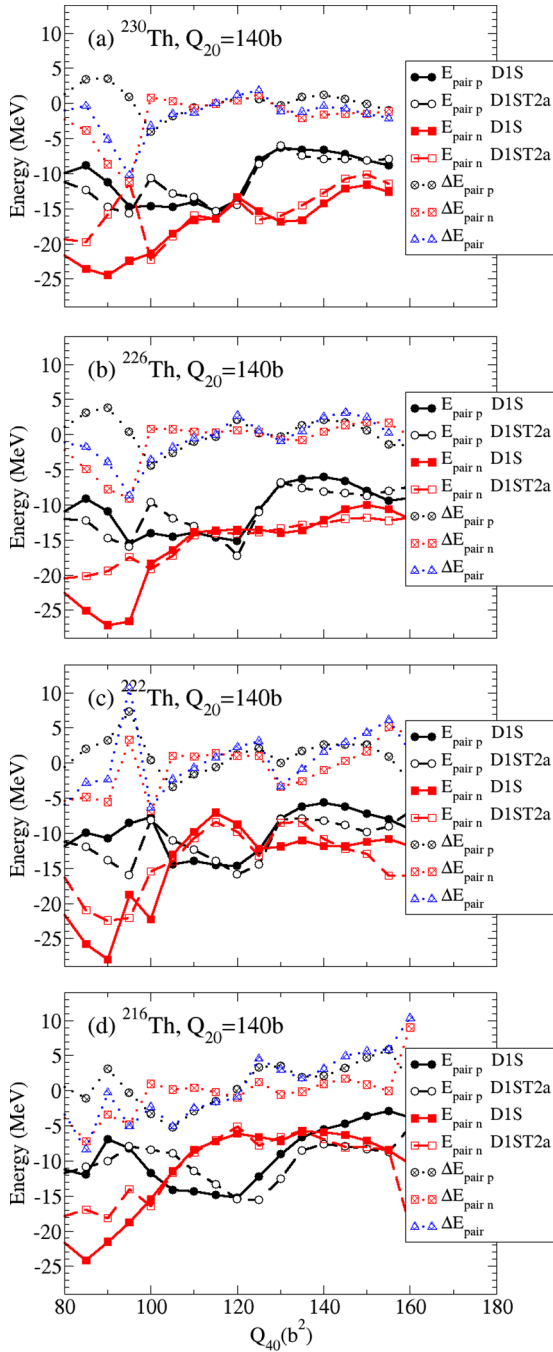
FIG. 15. Evolution of proton and neutron pairing components for both the D1S (black full circles and red full squares, respectively) and D1ST2a (black empty circles and red empty squares, respectively) interactions. The proton $\Delta E_{\mathrm{pair\,p}}$ and neutron $\Delta E_{\mathrm{pair\,n}}$ differences between both interactions (black dashed circles and red dashed squares are also indicated. The total difference ΔE_{pair} is shown in blue dashed triangles. Calculations have been done for (a) ^{230}Th, (b) ^{226}Th, (c) ^{222}Th, and (d) ^{216}Th at $Q_{20} = 140$ b. Energies are expressed in MeV.

to these correlations, as, for example, the collective masses which are crucial for the dynamical propagation. In Fig. 15, we report the evolution of the proton and neutron pairing components for both the D1S (full black circles and full red

squares, respectively) and D1ST2a (empty black circles and empty red squares, respectively) interactions. Moreover, the proton $\Delta E_{\mathrm{pair\,p}}$ and neutron $\Delta E_{\mathrm{pair\,n}}$ differences between both interactions (dashed black circles and dashed red squares, respectively) are also drawn. Finally, the total difference ΔE_{pair} in shown with dashed blue triangles. Calculations have been done for (a) ^{230}Th, (b) ^{226}Th, (c) ^{222}Th, and (d) ^{216}Th. As an example, the figure shows results for $Q_{20} = 140$ b. One observes a similar trend for all the isotopes. From the fusion-fission ridge and the V2-V1 ridge (A area), there is an increase of ΔE_{pair}. Then, a decrease is obtained between the V2-V1 ridge and the bottom of the valley V1 (B area) and finally a new increase for larger value of Q_{40} (C area) manifests. Looking at the proton and neutron decomposition, one sees that the variation ΔE_{pair} in the A area is mainly due to the proton pairing variation. The neutron one is nearly constant and close to zero. The proton variation changes sign whereas the neutron one is positive. In the B area, both proton and neutron variations decrease and participate in the total decrease which is found moderate. In the C area, the behavior of ΔE_{pair} in terms of proton and neutron components depends on the nucleus.

The neutron pairing energy along the isotopic chain is found to be very similar for both interactions in the region of the valley V2, with a value that changes a lot from isotope to isotope. Indeed, one observes a strong decrease from the heaviest to the lightest thorium isotopes. However, some variations appear in the valley V1. Concerning the proton pairing energy, differences in both the A and B areas are observed. In general, the proton pairing is larger in the A area and smaller in the B area with the D1S interaction

D. Distribution of the available energy at scission and neutron multiplicity

In this section we discuss the way the available energy of the fissioning system is distributed among the various physical components at scission. The available energy is defined as the difference between the total energy of the fissioning nucleus E_{tot} and the sum of the ground-state energy of fragments $E_{\mathrm{frag}}^{\mathrm{g.s.}}$. At scission, the available energy goes into two contributions: the total kinetic energy (TKE) and the total excitation energy (TXE),

$$E_{\mathrm{tot}} - E_{\mathrm{frag}}^{\mathrm{g.s.}} = \mathrm{TKE} + \mathrm{TXE}. \qquad (8)$$

The TKE takes most of the available energy and it is dominated by the Coulomb repulsion E_{Coul} energy between the fragments. The remaining part is known as the pre-kinetic energy E_{prek}. Concerning the TXE, it is the sum of the deformation energy E_{def} of the fragments and their intrinsic excitation energy E_{intr}. Thus,

$$E_{\mathrm{tot}} = E_{\mathrm{Coul}} + E_{\mathrm{prek}} + E_{\mathrm{def}} + E_{\mathrm{intr}} + E_{\mathrm{frag}}^{\mathrm{g.s.}}. \qquad (9)$$

In the present study, as we discuss low energy fission, we choose the total energy E_{tot} as the HFB energy obtained at the saddle point. Here, the scission point is defined when a sudden drop of the density between pre-fragments occurs. All the quantities involved in the energy distribution are evaluated in the first point of the PES mesh when the fragments appear.

TABLE IX. TKE and TXE evaluated at the exit point in the symmetric valley for the ^{230,226,222,216}Th isotopes. Coulomb, deformation energies and neutron multiplicities are added. Labels refer to the 3 scenarios. See text for explanations. Calculations have been done with the D1S Gogny force. Energies are expressed in MeV.

Nucleus	Valley	TKE$_1$	TKE$_2$	TKE$_3$	E_{coul}	TXE$_1$	TXE$_2$	TXE$_3$	E_{def}	ν_1	ν_2	ν_3
^{230}Th	V1	178.7	170.4	157.8	157.8	15.4	23.6	36.3	15.4	$\sim$1	1	2
^{226}Th	V1	178.0	170.3	157.2	157.2	14.2	21.9	35.0	14.2	0	1	2
^{222}Th	V1	177.0	169.1	156.5	156.5	14.8	22.8	35.3	14.8	0	1	2
^{216}Th	V1	182.3	177.8	157.2	157.2	8.2	12.6	33.3	8.2	0	0	1
					D1S, Symmetric path.							

The Coulomb energy is calculated at the scission point using the simple Coulomb formula:

$$E_{\text{Coul}} = \frac{Z_1 Z_2 e^2}{d_{\text{ch}}}, \qquad (10)$$

where Z_1 and Z_2 define the charge of the two fragments and d_{ch} is the distance between the center of mass of the charge distributions of the fragments at the exit point. Coulomb energies obtained for the symmetric valleys and for the four thorium isotopes are reported in Table IX (D1S) and Table X (D1ST2a). The Coulomb energy is almost isotope independent for the results with D1S due to the fact that the scission point are in the same quadrupole moment region (see Table V). The same conclusion apply for the D1ST2a interaction in valley V2 (see Table VI). However, in the V1 valley and with the D1ST2a interaction we find that the heavier the thorium isotope, the larger the elongation for the scission point. As a result, the distance d_{ch} is larger for heavy isotopes and the Coulomb energy is smaller. Coulomb energies from valley V2 are always bigger than the ones in valley V1 since their exit point occur at a smaller deformation.

The energies of the fragments at scission E_{frag} and the corresponding energies when the two fragments are well separated $E_{\text{frag}}^{\text{g.s.}}$ are obtained by means of HFB calculations. The deformation energy E_{def} is the differences between these two energies. Quadrupole and octupole moments from the fragments at scission are used as constraints to get the fragment HFB energy E_{frag}. The symmetric fission in the ^{230}Th, ^{226}Th, ^{222}Th, and ^{216}Th isotopes leads to ^{115}Rh, ^{113}Rh, ^{111}Rh, and ^{108}Rh fragments, respectively. In this work, the equal filling approximation has been used to calculate both the ground state and the deformed Rhodium isotopes using the same kind of methodology as the one reported in Ref. [77]

for odd and odd-odd nuclei. Fragment deformation energies E_{def} are depicted in Tables IX and X. As expected, in both calculations with D1S and D1ST2a, the deformation energy is bigger for more elongated fission. The most striking feature is that D1ST2a provides more deformation energy than D1S. This is expected when the scission point elongation is bigger for D1ST2a than D1S such as for ^{230}Th and ^{226}Th but it remains true when the elongation is about the same (^{222}Th) or is smaller (^{216}Th). Besides, for D1ST2a, deformation energies from valley V2 are significantly smaller than the ones in valley V1 by a factor 4.

Once Coulomb and fragment energies are calculated, Eq. (9) provides the quantity $E_{\text{prek}} + E_{\text{intr}}$ that are discussed in the following. Since quasi-particle excitation is not considered in this work to build PES, a microscopic evaluation of the part of the total available energy which is converted to intrinsic excitation is out of the scope of this work. Such a task using the Generator Coordinate Method framework would require the use of a non adiabatic model such as in Ref. [10]. We thus introduce three different scenarios about the way the energy is shared between the pre-kinetic and intrinsic energies and thus between the TKE and the TXE. Scenario 1 is defined as the one in which all the available energy $E_{\text{prek}} + E_{\text{intr}}$ goes to the pre-kinetic energy: $E_{\text{intr}} = 0$ MeV. In the second scenario, the intrinsic energy is chosen according to the empirical formula $E_{\text{intr}} = 35\%$TXE used in Refs. [66,78,79]. Contrary to scenario 1, in scenario 3, all the available energy goes to the intrinsic energy exclusively: $E_{\text{prek}} = 0$ MeV. Even if they may not be realistic in some cases, scenarios 1 and 3 provide boundaries for the quantities under consideration. For the three scenarios, the TKE and TXE has been obtained and given in Tables IX and X. For D1S, scenarios 1 and 2 look very similar: the TKE is stable for the three heaviest isotopes

TABLE X. Same as Table IX but for the D1ST2a Gogny interaction.

Nucleus	Valley	TKE$_1$	TKE$_2$	TKE$_3$	E_{coul}	TXE$_1$	TXE$_2$	TXE$_3$	E_{def}	ν_1	ν_2	ν_3
^{230}Th	V1	167.7	153.2	151.3	151.3	26.8	41.3	43.2	26.8	1	2	2
^{226}Th	V1	171.8	161.0	152.4	152.4	20.0	30.7	39.4	20.0	1	$\sim$2	2
	V2	**186.3**	**183.3**	**173.7**	**173.7**	**5.4**	**8.4**	**18.0**	5.4	**0**	**0**	**1**
^{222}Th	V1	175.1	166.8	156.1	156.1	15.5	23.9	34.5	15.5	0	1	2
	V2	**187.5**	**185.7**	**171.8**	**171.8**	**3.2**	**4.9**	**18.9**	3.2	**0**	**0**	**1**
^{216}Th	V1	180.0	174.7	160.8	160.8	9.8	15.1	29.0	9.8	0	$\sim$1	1
	V2	**187.5**	**186.2**	**172.1**	**172.1**	**2.4**	**3.7**	**17.8**	2.4	**0**	**0**	**1**
					D1ST2a, Symmetric path.							

TABLE XI. Experimental S_n^{exp} and theoretical $S_n^{D1S,D1ST2a}$ one-neutron separation energy S_n in Rhodium isotopes. Energies are expressed in MeV.

Isotope	^{115}Rh	^{114}Rh	^{113}Rh	^{112}Rh	^{111}Rh
S_n^{D1S}	6.224	4.918	7.139	5.174	7.654
S_n^{D1ST2a}	6.907	4.771	7.321	5.075	7.638
S_n^{exp}	6.590	5.020	7.110	5.500	7.547
Isotope	^{110}Rh	^{109}Rh	^{108}Rh	^{107}Rh	^{106}Rh
S_n^{D1S}	5.606	8.194	5.480	8.168	6.084
S_n^{D1ST2a}	5.476	8.067	5.898	8.605	4.569
S_n^{exp}	5.900	8.039	6.239	8.573	

and becomes significantly bigger for ^{216}Th. In a consistent way, the TXE is almost constant and decreases for ^{216}Th. In scenario 3 the TKE and TXE remain almost constant along the isotopic chain. For the D1ST2a interaction, the TKE is always driven by the Coulomb energy: for all the scenarios it increases with the isotope exoticism in valley V1 and is stable in valley V2. The three TXE are driven by the deformation energy which decreases with the mass number. Since the deformation energy is small in valley V2, scenario 2 is much closer to scenario 1 than scenario 3 for both TXE and TKE.

The TKE have been measured in Ref. [80] for ^{226}Th. The super long symmetric mode gives TKE $\simeq 160$ MeV close to scenario 3 for D1S (157.2 MeV) and scenario 2, valley V1 (161.0 MeV) for D1ST2a. This latter valley is the one energetically preferred for this isotope. In Ref. [64] the overall mean TKE in the thorium chain from ^{229}Th to ^{221}Th is given. It is stable along the symmetric/asymmetric transition with $\langle$TKE$\rangle = 167.7 \pm 3.4$ for ^{226}Th and $\langle$TKE$\rangle = 166.9 \pm 3.3$ for ^{222}Th. A comparison with the mean TKE will be possible in the future by solving the TDGCM equations with the static PES.

We now focus on the number of neutrons that are emitted at the exit points in all the symmetric valleys. Scission ends up with two similar fragments and the neutron multiplicity has been calculated for each of them. First, one has made the assumption that all the available energy from the TXE transforms itself into neutron emission. Once all the possible neutrons are emitted, the rest of the TXE would be devoted to γ emission, whose description is beyond the scope of this work. To account for γ emission, GCM + particle number projections techniques [81–84] should be used on each of the fragments. Thus, the TXE writes as

$$\text{TXE} = \sum_{i=1}^{2} E_\gamma^{(i)} + \nu^{(i)}\langle E_n^{(i)}\rangle + \sum_{j=1}^{\nu^{(i)}} S_n^{(j)} \qquad (11)$$

where $E_\gamma^{(i)}$ is the part of energy used to emit γ in fragment i, $\langle E_n^{(i)}\rangle$ is the mean neutron kinetic energy, $S_n^{(j)}$ are the successive one neutron separation energy of the fragment up to the post neutron emission fission product: $S_n^{(j)} = S_n(Z_{\text{frag}}, N_{\text{frag}} - j + 1)$. symmetric fission, the summation over the fragment's label i in Eq. (11) can be replaced by an overall factor 2. Separation energies are presented in Table XI. A comparison of D1S and D1ST2a HFB calculations with experimental

TABLE XII. Mean neutron kinetic energy $\langle E_n^{(i)}\rangle$ extracted from GEF. Energies are expressed in MeV.

Isotope	^{230}Th	^{226}Th	^{222}Th	^{216}Th
$\langle E_n^{(i)}\rangle$	1.924	1.814	1.855	1.852

data leads to the conclusion that both interactions give a satisfactory agreement with experiment with a deviation of a few hundred keV.

Mean neutron kinetic energies $\langle E_n^{(i)}\rangle$ are displayed in Table XII. These quantities are evaluated using the GEF model of Ref. [79] for a neutron incident energy at the barrier.

The neutron multiplicity of each fragment $\nu^{(i)}$ is extracted from Eq. (11) as the biggest integer which satisfies:

$$\text{TXE} \geqslant \sum_{i=1}^{2} \nu^{(i)}\langle E_n^{(i)}\rangle + \sum_{j=1}^{\nu^{(i)}} S_n^{(j)} \qquad (12)$$

Neutron multiplicities $\nu^{(i)}$ for each fragment are reported in Tables IX and X for all the three different scenarios. A tilde is used when less than 500 keV are missing in the TXE to reach the next integer value. The $\nu^{(i)}$ globally decrease with the mass number for both interactions. The valley V2 does not provide neutron emission, except for scenario 3.

The emergence of the second symmetric valley V2 leads to a bigger TKE than for the first valley V1 and thus a smaller TXE. A drop of the experimental $\langle \nu_{\text{tot}}\rangle$ for symmetric fission is expected when going to light thorium isotopes.

As already mentioned for D1ST2a, the second valley V2 is not energetically favored in the ^{226}Th and ^{222}Th isotopes, contrary to the ^{216}Th case. When comparing ^{222}Th or ^{216}Th(valley V2) with ^{230}Th (valley V1) the Coulomb energy E_{coul} is higher by $\simeq 20$ MeV in the lighter isotopes. This additional kinetic energy corresponding to a compact scission mode results in a drop of the TXE which leads to a loss of 1 neutron per fragment for scenario 1 and 3, and 2 neutrons per fragment for scenario 2. It is in agreement with the loss of 2–2.5 neutrons on the total multiplicity which has been measured by the SOFIA group [58,59].

IV. CONCLUSION AND PERSPECTIVES

In this work, the effect of the tensor term on fission paths has been studied for the first time. In that context, we have investigated the asymmetric to symmetric fission transition in the light thorium isotopes which experimentally hints to the existence of a new, compact and symmetric, fission mode. We have used a static calculation based on an axial HFB approach breaking reflection symmetry and introducing constraints on multipole moments and particle numbers. Both, the D1S and the D1ST2a (D1S plus a perturbative finite range tensor) Gogny interactions have been used.

We have shown that, depending on the isotope, the tensor term can change the barrier height in a non negligible way. In particular, it is able to re-equilibrate the second hump height between the asymmetric and symmetric path. Indeed, in the ^{222}Th isotope, this difference with the D1S interaction has

been found equal to $\simeq 4$ MeV whereas it is reduced to 1.5 MeV with the D1ST2a interaction. Thus, the tensor interaction renders the pure symmetric path more probable. In the ^{216}Th isotope, this difference disappears.

Another striking feature is the appearance of a second valley in the $\{Q_{20}, Q_{40}\}$ collective variables in the presence of the tensor term. Its existence and its deformation characteristics (much smaller values of Q_{20} and Q_{40} than the ones of the standard valley which leads to the known well-elongated symmetric fission) are interpreted as the theoretical proof of the experimentally observed symmetric compact fission mode. It is the most remarkable result of this analysis.

The present study does not consider the dynamical aspects of fission and therefore cannot predict fission fragment mass distributions. To describe the population of the various valleys, it will be very interesting to perform a three-dimensional dynamical calculations including Q_{20}, Q_{30}, and Q_{40} as collective variables. Moreover, it would be crucial to perform systematic calculations to localize the possible areas where the tensor term is expected to play an important role for fission process. Finally, a full refit of the Gogny interaction including a finite range tensor term would be of prime interest.

[1] N. Schunck and L. M. Robledo, Rep. Prog. Phys. **79**, 116301 (2016).

[2] W. Younes, D. M. Gogny, and J.-F. Berger, *A Microscopic Theory of Fission Dynamics Based on the Generator Coordinate Method*, Lecture Notes in Physics 950 (Springer, Berlin, 2019).

[3] J.-F. Berger, M. Girod, and D. Gogny, Nucl. Phys. A **428**, 23 (1984).

[4] J.-F. Berger, M. Girod, and D. Gogny, Nucl. Phys. A **502**, 85 (1989).

[5] H. Goutte, J. F. Berger, P. Casoli, and D. Gogny, Phys. Rev. C **71**, 024316 (2005).

[6] N. Dubray, H. Goutte, and J.-P. Delaroche, Phys. Rev. C **77**, 014310 (2008).

[7] W. Younes and D. Gogny, Phys. Rev. C **80**, 054313 (2009).

[8] W. Younes and D. Gogny, Phys. Rev. Lett. **107**, 132501 (2011).

[9] S. A. Giuliani and L. M. Robledo, Phys. Lett. B **787**, 134 (2018).

[10] R. Bernard, H. Goutte, D. Gogny, and W. Younes, Phys. Rev. C **84**, 044308 (2011).

[11] M. Warda and A. Zdeb, Phys. Scr. **90**, 114003 (2015).

[12] D. Regnier, N. Dubray, N. Schunck, and M. Verriere, Phys. Rev. C **93**, 054611 (2016).

[13] W. Younes, Eur. Phys. J. A **53**, 109 (2017).

[14] A. Zdeb, A. Dobrowolski, and M. Warda, Phys. Rev. C **95**, 054608 (2017).

[15] G. F. Bertsch, W. Younes, and L. M. Robledo, Phys. Rev. C **97**, 064619 (2018).

[16] D. Regnier, N. Dubray, and N. Schunck, Phys. Rev. C **99**, 024611 (2019).

[17] G. Scamps and C. Simenel, Nature **564**, 382 (2018).

[18] Y. Tanimura, D. Lacroix, and S. Ayik, Phys. Rev. Lett. **118**, 152501 (2017).

[19] Y. Tanimura, D. Lacroix, and S. Ayik, Phys. Rev. Lett. **121**, 059902(E) (2018).

[20] A. Bulgac, P. Magierski, K. J. Roche, and I. Stetcu, Phys. Rev. Lett. **116**, 122504 (2016).

[21] H. Flocard, P. Quentin, D. Vautherin, M. Veneroni, and A. K. Kerman, in *Proc. IAEA Symp. Phys. Chem. of Fission, Rochester, 1973* (IAEA, Vienna, 1974), Vol. I, p. 221.

[22] H. Flocard, P. Quentin, D. Vautherin, M. Veneroni, and A. K. Kerman, Nucl. Phys. A **231**, 176 (1974).

[23] J. W. Negele, S. E. Koonin, P. Moller, J. R. Nix, and A. J. Sierk, Phys. Rev. C **17**, 1098 (1978).

[24] M. Brack, in *Proc. IAEA Symp. Phys. Chem. of Fission, Julich, 1979* (IAEA, Vienna, 1980), Vol. I, p. 227.

[25] A. K. Dutta and M. Kohno, Nucl. Phys. A **349**, 455 (1980).

[26] D. Gogny, in *Proceedings of the International Conference on Nuclear Physics* (Elsevier, Munich, August 27–September 1, 1973).

[27] J. Dechargé and D. Gogny, Phys. Rev. C **21**, 1568 (1980).

[28] D. Gogny, *Nuclear Self-Consistent Fields*, Trieste, edited by G. Ripka and M. Porneuf (North-Holland, Amsterdam, 1975), p. 333.

[29] J. Coté and J. M. Pearson, Nucl. Phys. A **304**, 104 (1976).

[30] J.-F. Berger, M. Girod, and D. Gogny, Comput. Phys. Commun. **63**, 365 (1991).

[31] M. Girod, D. Gogny, and B. Grammaticos, in *7 Ième Session D'études Biennale de Physique Nucléaire (Aussois, 14–18 Mars 1983)* (IPN, Lyon, 1983).

[32] M. Brack, J. Damgaard, A. S. Jensen, H. C. Pauli, V. M. Strutinsky, and C. Y. Wong, Rev. Mod. Phys. **44**, 320 (1972).

[33] G. Bertsch and H. Flocard, Phys. Rev. C **43**, 2200 (1991).

[34] L. G. Moretto and R. P. Babinet, Phys. Lett. B **49**, 147 (1974).

[35] S. A. Giuliani, L. M. Robledo, and R. Rodríguez-Guzmán, Phys. Rev. C **90**, 054311 (2014).

[36] R. Bernard, S. A. Giuliani, and L. M. Robledo, Phys. Rev. C **99**, 064301 (2019).

[37] L. M. Robledo *et al.*, J. Phys. G: Nucl. Part. Phys. **46**, 013001 (2019).

[38] S. Péru and M. Martini, Eur. Phys. J. A **50**, 88 (2014).

[39] T. Lesinski, M. Bender, K. Bennaceur, T. Duguet, and J. Meyer, Phys. Rev. C **76**, 014312 (2007).

[40] M. Bender, K. Bennaceur, T. Duguet, P.-H. Heenen, T. Lesinski, and J. Meyer, Phys. Rev. C **80**, 064302 (2009).

[41] T. Otsuka, T. Matsuo, and D. Abe, Phys. Rev. Lett. **97**, 162501 (2006).

[42] M. Anguiano, G. Cò, V. De Donno, and A. M. Lallena, Phys. Rev. C **83**, 064306 (2011).

[43] M. Anguiano, M. Grasso, G. Cò, V. De Donno, and A. M. Lallena, Phys. Rev. C **86**, 054302 (2012).

[44] M. Grasso and M. Anguiano, Phys. Rev. C **88**, 054328 (2013).

[45] M. Anguiano, A. M. Lallena, G. Cò, V. De Donno, M. Grasso, and R. N. Bernard, Eur. Phys. J. A **52**, 183 (2016).

[46] R. N. Bernard and M. Anguiano, Nucl. Phys. A **953**, 32 (2016).

[47] M. Maire, Etude Des Propriétés De L'état Fondamental Des Noyaux Sphériques, Par La Méthode Des Perturbations, Avec Une Interaction Nucléon-Nucléon Réaliste Et Non Singulière, Thèse de doctorat, Université Paris-Sud, Orsay, France, 1976.

[48] D. Gogny, P. Pires, and R. de Tourreil, Phys. Lett. B **32**, 591 (1970).

[49] F. Chappert, N. Pillet, M. Girod, and J.-F. Berger, Phys. Rev. C **91**, 034312 (2015).

[50] N. Pillet and S. Hilaire, Eur. Phys. J. A **53**, 193 (2017).

[51] K. Sekizawa and K. Yabana, Phys. Rev. C **93**, 054616 (2016).

[52] L. Guo, C. Simenel, L. Shi, and C. Yu, Phys. Lett. B **782**, 401 (2018).

[53] L. Guo, K. Godbey, and A. S. Umar, Phys. Rev. C **98**, 064607 (2018).

[54] K. Godbey, L. Guo, and A. S. Umar, Phys. Rev. C **100**, 054612 (2019).

[55] P. D. Stevenson and M. C. Barton, Prog. Part. Nucl. Phys. **104**, 142 (2019).

[56] J.-F. Martin *et al.*, Eur. Phys. J A **51**, 174 (2015).

[57] E. Pellereau *et al.*, Phys. Rev. C **95**, 054603 (2017).

[58] A. Chatillon *et al.*, Phys. Rev. C **99**, 054628 (2019).

[59] A. Chatillon *et al.* (unpublished).

[60] C. Simenel and A. S. Umar, Prog. Part. Nucl. Phys. **103**, 19 (2018).

[61] R. Bernard, unpublished HFBaxialT computer code (2018).

[62] J. L. Egido, L. M. Robledo, and R. R. Chasman, Phys. Lett. B **393**, 13 (1997).

[63] L. M. Robledo and G. F. Bertsch, Phys. Rev. C **84**, 014312 (2011).

[64] K. H. Schmidt *et al.*, Nucl. Phys. A **665**, 221 (2000).

[65] A. Andreyev *et al.*, Phys. Rev. Lett. **105**, 252502 (2010).

[66] M. Caamaño and F. Farget, Phys. Lett. B **770**, 72 (2017).

[67] J. Khuyagbaatar *et al.*, Phys. Rev. Lett. **115**, 242502 (2015).

[68] J. O. Rasmussen, Phys. Rev. **113**, 1593 (1959).

[69] J.-P. Delaroche, M. Girod, J. Libert, H. Goutte, S. Hilaire, S. Peru, N. Pillet, and G. F. Bertsch, Phys. Rev. C **81**, 014303 (2010).

[70] http://www-phynu.cea.fr/science_en_ligne/carte_potentiels_microscopiques/tables/HFB-5DCH-table.htm

[71] J. Blons, C. Mazur, D. Paya, M. Ribrag, and H. Weigmann, Nucl. Phys. A **414**, 1 (1984).

[72] J. Blons, B. Fabbro, C. Mazur, D. Paya, M. Ribrag, and Y. Patin, Nucl. Phys. A **477**, 231 (1988).

[73] J. Blons, Nucl. Phys. A **502**, 121 (1989).

[74] J. Blons, Thèse d'état, *Etats Asymétriquement Déformés Des Isotopes De Thorium Au Cours Du Processus De Fission*, Université Paris-Sud centre d'Orsay (1982).

[75] P. Romain, B. Morillon, and H. Duarte, Nucl. Dat. Sheets **131**, 222 (2016).

[76] D. Regnier, N. Dubray, M. Verriere, and N. Schunck, Com. Phys. Com. **225**, 180 (2018).

[77] L. M. Robledo, R. N. Bernard, and G. F. Bertsch, Phys. Rev. C **86**, 064313 (2012).

[78] F. Rejmund, A. V. Ignatyuk, A. R. Junghans, and K.-H. Schmidt, Nucl. Phys. A **678**, 215 (2000).

[79] K.-H. Schmidt, B. Jurado, C. Amouroux, and C. Schmitt, Nucl. Data Sheets **131**, 107 (2016).

[80] C. Böckstiegel *et al.*, Nucl. Phys. A **802**, 12 (2008).

[81] T. R. Rodríguez and J. L. Egido, Phys. Rev. Lett. **99**, 062501 (2007).

[82] M. Bender and P.-H. Heenen, Phys. Rev. C **78**, 024309 (2008).

[83] J. M. Yao, J. Meng, P. Ring, and D. Vretenar, Phys. Rev. C **81**, 044311 (2010).

[84] R. N. Bernard, L. M. Robledo, and T. R. Rodríguez, Phys. Rev. C **93**, 061302(R) (2016).

Correction: Figure 9 was processed improperly during the production cycle and has been fixed.

Second Correction: Figure 9(d) contained an error in the description label and has been replaced. Reference [60] and its citation in Sec. II A were missing and have been inserted.